Applied Clay Science 241 (2023) 107002

Contents lists available at ScienceDirect

Applied Clay Science

journal homepage: www.elsevier.com/locate/clay

Research Paper

Allantoin-zinc layered simple hydroxide biohybrid as antimicrobial active phase in cellulosic bionanocomposites as potential wound dressings

Esther Marugan [a], Ediana P. Rebitski [a], Margarita Darder [a,*], Salvador R.G. Balestra [b], Gustavo del Real [c], Pilar Aranda [a,*]

[a] Instituto de Ciencia de Materiales de Madrid (ICMM), CSIC, 28049 Madrid, Spain
[b] Departmento de Sistemas Físicos, Químicos y Naturales, Universidad Pablo de Olavide, ES-41013 Seville, Spain
[c] Instituto Nacional de Investigación y Tecnología Agraria y Alimentaria (INIA), CSIC, Ctra. de la Coruña km 7, 5, 28040 Madrid, Spain

ARTICLE INFO

Keywords:
Allantoin
Layered simple hydroxide
Zinc
Cellulose
Antibacterial activity
Wound healing

ABSTRACT

Cellulosic materials loaded with a novel zinc layered simple hydroxide (LSH) with allantoin in its structure (allant-ZnLSH) have been developed for potential application as wound dressings. The allant-ZnLSH biohybrid was synthesized by slow addition of a zinc chloride solution to an aqueous solution of allantoin, while adding a NaOH solution dropwise to maintain a controlled pH. The recovered precipitate was characterized by XRD, FTIR, chemical analysis, and FE-SEM. The allant-ZnLSH material was further incorporated into biopolymeric matrices such as hydroxypropylmethylcellulose (HPMC), carboxymethylcellulose (CMC) and cellulose nanofibers (CNF), because of their biocompatibility and biodegradability. The resulting films presented suitable mechanical properties, with Young's modulus values ranging between 1.3 and 3.9 GPa, as well as appropriate water vapor transmission rates (WVTR) for application in would healing, around 250–630 g/m^2 per day. The bionanocomposite films also showed interesting barrier properties against the passage of UV light, while keeping a certain transparency in the visible range that would allow the healing process to be monitored without removing the dressing. Their antibacterial action was evaluated against *E. coli* and *S. aureus* in agar plates, showing only antimicrobial activity against the latter. The goal is to develop materials that can exhibit antimicrobial, and skin regenerative properties provided by the presence of zinc ions and allantoin, respectively.

1. Introduction

Wound dressings were considered only a passive barrier until the 1960s, but today the goal is to develop dressings capable of actively participating in the healing process and promoting it. Thus, functional dressings are designed to create an optimal environment, in terms of moisture and healing, and providing antibacterial activity to protect the wounded skin from infection (Boateng et al., 2008; Dhivya et al., 2015). Functionalized dressings are commonly prepared by incorporating antimicrobial agents to polymer supports, either directly (Maver et al., 2015) or previously loaded in organic or inorganic nanocarriers from which they can be slowly released to produce a more controlled and sustained activity (Saghazadeh et al., 2018). In the latter case, clay minerals including smectites, sepiolite, palygorskite or halloysite have been widely used as drug nanocarriers for wound dressings and related biomedical applications (García-Villén et al., 2020; Lisuzzo et al., 2020; Stavitskaya et al., 2019), and more recently the research on this topic has been extended to hydrotalcite-like compounds, including layered double hydroxides (LDH) (Figueiredo et al., 2020, 2022; Perioli et al., 2019) as well as layered hydroxide salts or layered simple hydroxides (LSH) (Barahuie et al., 2014; Nabipour and Hu, 2022). These hydrotalcite-like materials, also known as anionic clays, offer numerous advantages including their low cost, the easy tuning of their chemical composition, and the ability to accommodate anions in the hydrated interlayer space of the metal hydroxide layers, which make them excellent materials for a wide range of applications from energy to medicine (Evans and Duan, 2006; Delahaye et al., 2010; Rogez et al., 2011; Yu et al., 2017). LSH materials show a brucite-like structure, comprising only one type of metal cation with the chemical structure $M_2(OH)_{4-x}(A^{n-})_{x/n}{\cdot}zH_2O$ (Delahaye et al., 2010). Although the interlayer anions are coordinated to the in-plane metal ions of the inorganic layers, they can be exchanged by other negatively charged organic species (Si et al., 2012), leading to novel hybrid materials for a wide range of applications. For instance, zinc-based LSH have been used as

* Corresponding authors.
E-mail addresses: darder@icmm.csic.es (M. Darder), pilar.aranda@csic.es (P. Aranda).

https://doi.org/10.1016/j.clay.2023.107002
Received 10 February 2023; Received in revised form 9 May 2023; Accepted 19 May 2023
Available online 6 June 2023

nanocarriers of herbicides (Hussein et al., 2012) or different types of drugs (Nabipour and Hu, 2022) to develop controlled release formulations, UV-blocking molecules for sunscreen application (Mohsin et al., 2013), or niobate complexes for potential production of biodiesel (Arizaga et al., 2009). Regarding the topic of wound healing, an interesting feature of layered hydroxides is the possibility of tuning their composition incorporating in the structure cations with antibacterial activity such as zinc (León-Vallejo et al., 2019) as an alternative to the use of antibiotic drugs accommodated in their interlayer space (Figueiredo et al., 2020, 2022). The antimicrobial activity reported for various zinc-based materials such as ZnO nanoparticles or Zn-based metal-organic frameworks (MOFs) has been attributed to several mechanisms involving the released Zn^{2+} cations or the generation of reactive oxygen species (ROS) (Li et al., 2012; Riduan and Zhang, 2021).

Among the different types of wound dressings, biopolymer-based dressings offer several advantages such as biocompatibility and biodegradability, suitable water vapor permeability, ability to maintain a suitable moist environment in the injured area and to absorb exudates, possibility to incorporate drugs or antimicrobial agents for their controlled release, as well as transparency to monitor the evolution of the wound during the healing process (Koehler et al., 2018; Liang et al., 2021; Smith et al., 2016). There are numerous examples in the literature about the formation of dressings from very abundant polysaccharides such as alginates, chitosan, pectins or cellulose among others (Kuznetsova et al., 2020; Liang et al., 2021; Portela et al., 2019). Bionanocomposite materials developed by dispersion of nanoparticles within these polysaccharides and other natural polymers (Darder et al., 2007; Ruiz-Hitzky et al., 2008) are also good candidates for application as wound dressings (Perioli et al., 2019; Kanikireddy et al., 2020; Lisuzzo et al., 2020). Cellulose is the most abundant polysaccharide on Earth and it is an important source of materials for biomedical applications, including not only plant-derived cellulose nanofibrils but also other cellulose derivatives such as hydroxypropylmethylcellulose (HPMC) or carboxymethylcellulose (CMC) (Kanikireddy et al., 2020; Rashki et al., 2021; Tarrahi et al., 2022). Nanofibrillated cellulose, also known as cellulose nanofibers (CNF), is one of the most versatile materials obtained from cellulose pulp by mechanical and chemical treatments, being TEMPO-mediated oxidation and diverse mechanical treatments (high-pressure microfluidization, grinding, *etc.*) the most widely used procedures, which are commonly applied in combination (Abdul Khalil et al., 2014; Fillat et al., 2018; Isogai et al., 2011). CNF, HPMC and CMC are good candidates to develop sustainable wound dressings due to their good film-forming ability, transparency, flexibility, good mechanical properties, and the possibility of being easily functionalized or integrated in composite materials to offer antimicrobial activity (Amalraj et al., 2018; Dharmalingam and Anandalakshmi, 2019; Kanikireddy et al., 2020; Rashki et al., 2021).

Current research on wound dressings tends towards the development of functionalized materials that incorporate drugs or components with beneficial therapeutic properties for skin repair, such as allantoin. This biomolecule, also known as (2,5-dioxo-4-imidazolidinyl) urea or 5-ureidohydantoin, is a nitrogenous amphoteric molecule derived from the oxidation of uric acid present in mammalian urine or in snail slime, and also produced by certain plants such as *aloe vera* or comfrey, which can also be prepared synthetically in large quantities (Becker et al., 2010; Ferreira et al., 2022). Allantoin is used in a wide variety of cosmetic products, such as shaving creams and foams, aftershaves, shampoos, *etc.*, due to its moisturizing, keratolytic, soothing and anti-irritant properties and its ability to promote cell regeneration (Becker et al., 2010; Ferreira et al., 2022). Its ability to accelerate wound healing has been confirmed also from *in vivo* studies carried out in rats (Araújo et al., 2010). In addition, it has been shown that allantoin properties can be enhanced by binding to several metals such as zinc, silver, tin or copper, which increases its stability and can hasten the restoration of damaged skin (Klippel and Margraf, 1974; Pickart, 1995).

The current work reports the preparation of a novel zinc-LSH with allantoin in its structure (allant-ZnLSH) by controlled coprecipitation at basic pH, which is then dispersed within a cellulose-based matrix (HPMC, CMC or CNF) in order to develop bionanocomposite films for potential application as wound dressings. The properties of the final materials were evaluated for this purpose, and their antimicrobial activity was tested against *E. coli* and *S. aureus*, the latter being the main cause of skin infections in humans and animals.

2. Experimental section

2.1. Starting materials and reagents

Zinc chloride ($ZnCl_2$ reagent grade, > 98%) was obtained from Alfa Aesar. Allantoin (> 98%), hydroxypropylmethylcellulose (HPMC; ~22 kDa; *v*iscosity 40–60 cP measured in 2% in H_2O, 20 °C) and carboxymethylcellulose sodium salt (CMC; medium viscosity: 400–800 cps measured in 2% aqueous solution at 25 °C) in powder form, and $NaH_2PO_4{\cdot}H_2O$ (ACS reagent) were provided by Sigma-Aldrich. Sodium hydroxide (pellets, EMPLURA®) was obtained from Merck. The eucalyptus cellulose pulp was kindly provided by "La Montañanesa" (Lecta group, Zaragoza, Spain). For the preparation of nanofibrillated cellulose by chemical process the following reagents were used: 2,2,6,6-tetramethylpiperidin-1-oxyl (TEMPO, 98%), sodium bromide (NaBr, BioXtra >99%), and sodium hypochlorite solution (NaClO, reagent grade, active chlorine 1.57 mol/L), obtained from Sigma-Aldrich. Hydrochloric acid (HCl, 37%) was obtained from Laporte. Ultrapure water (conductivity <18.2 MΩ cm) was obtained from a Maxima Ultra Pure Water system from Elga.

2.2. Synthesis of the hybrid material allantoin/Zn-layered simple hydroxide (LSH)

The synthesis of the hybrid system of allantoin and zinc layered simple hydroxide (LSH) was carried out by controlled precipitation of zinc hydroxide in the presence of the organic molecule. Following the procedure described by Rebitski (2020), 15.58 mmol of $ZnCl_2$ were dissolved in 250 mL of bidistilled water and the allantoin solution was prepared in water at pH = 8–9, with magnetic stirring and under N_2 bubbling for at least 30 min. The $ZnCl_2$ aqueous solution was added dropwise at a rate of 2 mL/min, with the help of an automatic dispensing equipment (Dosino 800, Metrohm), to 200 mL of 1% (*w/v*) allantoin solution (corresponding to 12.6 mmol of allantoin), which was kept under a constant N_2 flow. Simultaneously, 1 M NaOH solution was added dropwise to the system to maintain a constant pH close to 9.0 during the synthesis, controlled automatically by the 867 pH Module by means of the pH sensor Unitrode 854 iConnect, and using the software Tiamo *v*2.3 from Metrohm. The resulting dispersion was kept under magnetic stirring and N_2 bubbling for 24 h to ensure complete precipitation and crystal growth of the allant-ZnLSH hybrid. The solid product obtained was isolated by centrifugation, washed three times with deionized water to ensure elimination of chloride ions, and dried at 60 °C.

2.3. Nanofibrillation of cellulose

Cellulose nanofibrils (CNF) were prepared from eucalyptus cellulose pulp, following the procedure described by Saito et al. (2007), where a chemical pretreatment was applied to the cellulose pulp before the microfluidization stage. Initially, the cellulose pulp was washed in HCl solution at pH 2 with constant stirring for 20 min, in order to remove possible heavy metals. Then, it was filtered with a Büchner funnel and washed with bidistilled water until neutral pH. For the chemical pretreatment, oxidation was carried out with sodium hypochlorite catalyzed by TEMPO. The reagents were added to an aqueous dispersion of the pulp around 1% *w/v* in the following order: TEMPO (0.016 g/g of pulp) and NaBr (0.1 g/g of pulp), and then NaClO (10 mmol/g of pulp).

NaOH solution (0.5 M) was added dropwise to maintain the pH at a constant value of 10 during the process. The oxidation ended when no change in pH was observed. Then, the pulp was vacuum filtered, washed with plenty of water (>5 L) to remove the added reagents and reach a neutral pH. Finally, it was redispersed in ultrapure water up to an approximate concentration of 1% *w/v*. An amount of carboxylic groups of 1.35 mmol/g was determined by conductometric titration with NaOH (Saito and Isogai, 2004), using a platinum conductivity cell 50–70 and a GLP 31 conductivity meter from Crison.

Subsequently, a mechanical treatment was carried out using a M-110P Microfluidizer (Microfluidics International Corporation). Previously, the sample was homogenized using high shear agitation (18,000 rpm) with a T25 digital Ultra-Turrax® from IKA for 5 min to reduce the fiber size and guarantee the absence of aggregates. Three passes were made using 200 μm and 100 μm chambers and applying pressures of 1,000 bar in the first and second passes, and 2,000 bar in the third one. Once the nanocellulose is obtained, the amount of water is determined by means of a moisture analyzer (HE53, Mettler Toledo), determining a CNF concentration of 0.97% *w/v*.

2.4. Preparation of bionanocomposite films by incorporation of the hybrid allantoin-ZnLSH in cellulosic matrices

HPMC and CMC films loaded with allant-ZnLSH were prepared by dissolving 2 g of polymer in 50 mL of water and dispersing a variable amount of allant-ZnLSH (Table 1) in 50 mL of water, which were slowly added to the polymer solution under magnetic stirring. After complete homogenization, the dispersions were placed in Petri dishes (50 mL per dish) and dried in a Climacell EVO climatic chamber (MMM Group) at 75% relative humidity and 35 °C.

In the case of CNF, several dispersions of allant-ZnLSH in 2 mL of bidistilled water (Table 1) were slowly added to 10 mL of a 0.5% *w/v* dispersion of CNF, until achieving homogeneous mixtures. The dispersions were then vacuum filtered using 0.45 μm pore size filters (mixed cellulose esters, Merck-Millipore). The hydrated films were separated from the filtration membrane and placed on a homemade pressing system that was left in a vacuum hood at 50 °C for approximately one hour. The resulting samples were labeled as CNF 0%; CNF 3.6%; CNF 9%; CNF 20% and CNF 33%.

2.5. Characterization

The prepared materials were characterized by X-ray powder diffraction (XRD) using a Bruker D8-ADVANCE diffractometer equipped with a "Lynxeye" detector, using the copper Kα line radiation with a goniometer speed of 0.3 s/step between 3 and 70 degrees of 2θ angle values. Fourier transform infrared spectroscopy (FTIR) was carried out using a Bruker Vertex 70 V spectrometer. Samples were diluted in KBr (~2%) and pelletized under a pressure of 10 tons, and the spectra recorded from 4000 to 400 cm^{-1} with 2 cm^{-1} resolution. Thermogravimetric (TG) and differential thermal analysis (DTA) curves were recorded simultaneously in an SDT Q600-TA equipment, from room temperature to 800 °C at a heating rate of 10 °C/min under air atmosphere (flow of 100 mL/min). Elemental chemical analysis (CHN) was carried out on a LECO CHNS-932 analyzer. Solid state $^{13}C\{^1H\}$ CP-MAS and $^{15}N\{^1H\}$ CP-MAS NMR experiments were carried out on a Bruker AV400 spectrometer operating at frequencies of 100.61, 40.55 and 400.13 MHz for ^{13}C, ^{15}N and ^1H, respectively (9.4 T). Samples were packed inside 4 mm zirconia rotors and spun at 10 kHz around an axis inclined 54°44′ with respect to the external magnetic field. Spectra were acquired using a CP-MAS sequence with contact times of 2 and 4 ms, recycle delays of 5 and 4 s and number of scans 720–1200 and 56,000 for $^{13}C\{^1H\}$ CP-MAS and $^{15}N\{^1H\}$ CP-MAS experiments, respectively. Field Emission Scanning Electron Microscopy (FESEM) was performed in a high-resolution FEI NOVA NANO 230 microscope equipped with an Apollo XL Silicon Drift Detector (SDD) from EDAX-Ametek. The powder samples were adhered on a carbon adhesive tape and directly visualized without the need for any conductive coating. In the case of films, they were coated for 25 s with a very thin gold layer using a Leica EM ACE200 coating system.

Table 1
Amounts of biopolymer and allant-ZnLSH hybrid used in the preparation of the bionanocomposite films.

Label	Amount of polymer (mg)	Allant-ZnLSH (mg)	% of hybrid (%*w/w*)
HPMC	2000	0	0
HPMC-3.6%	2000	75	3.6
HPMC-9%	2000	200	9
HPMC-20%	2000	500	20
HPMC-33%	2000	1000	33
CMC	2000	0	0
CMC-3.6%	2000	75	3.6
CMC-9%	2000	200	9
CMC-20%	2000	500	20
CMC-33%	2000	1000	33
CNF	50	0	0
CNF-3.5%	50	1.8	3.5
CNF-8.3%	50	4.5	8.3
CNF-16.7%	50	10.0	16.7
CNF-24.8%	50	16.5	24.8

2.6. Mechanical properties

The mechanical resistance to traction of the films was evaluated using a universal mechanical test machine (Model 3345, Instron). The samples were cut into strips (1 cm wide and about 5 cm long), placed between the jaws, and fixing the cross-head speed at 5 mm/min, with a load cell of 100 N. At least two measurements were made for each sample.

2.7. Water sorption isotherms

The absorption of moisture by the bionanocomposite films was studied using a dynamic water vapor analyzer Aquadyne DVS from Quantachrome, which records the variation of mass experienced by the sample as a function of the relative humidity of water vapor maintained in the test chamber. The adsorption/desorption isotherms were recorded at 25 °C in the range of relative humidity from 0% to 95%.

2.8. Water vapor transmission and permeability

The water vapor transmission rate (WVTR) and the water vapor permeability (WVP) were evaluated adapting the ASTM E96 standard, using the desiccant method. For this purpose, 14 g of dry silica gel were weighed in closed containers with a circular opening of 10 mm in diameter in their lids. The different films were placed over this opening and fixed to the lids using adhesive aluminum foil, also perforated with a 10-mm-diameter die. These containers were kept for 5 days in a controlled humidity chamber, keeping a relative humidity of 75% with a saturated NaCl solution, and they were weighed each day. The WVTR for each film was obtained from the slope of the representation of the mass of absorbed water (g) *vs.* time (day), and dividing the obtained value by the film area (m^2). WVP (g/Pa s m) was determined using the following equation:

$$WVP = \frac{WVTR \times L}{S \times (R_2 - R_1)} \quad (1)$$

where L is the film thickness (m), S: saturation vapor pressure at test temperature (23.77 mmHg or 3168.5 Pa at 25 °C), R_1: relative humidity of the silica gel (0%) and R_2: relative humidity of the container (75%). The measurements were made at least in duplicate for each film sample.

2.9. Water absorption capacity in simulated wound fluid

The water absorption capacity (WAC) of the bionanocomposite films was determined gravimetrically. For this purpose, weighed amounts of each film were kept in simulated wound fluid (SWF; 142 mM NaCl and 2.5 mM $CaCl_2$, pH ≈ 6) (Canada et al., 2011) at room temperature for 24 h. After this time, each film was removed from the SWF, the excess of liquid was removed from the surface with filter paper and then the wet film was weighed. The WAC was determined from the following equation:

$$WAC = \frac{(w_s - w_d)}{w_d} \times 100 \quad (2)$$

where w_d and w_s are the weights of the films in the dry and in the swollen state, respectively. The measurements were carried out in duplicate.

2.10. Optical properties

The optical properties of the bionanocomposite films were studied measuring their transmittance in the wavelength range of 800–200 nm using a UV–visible spectrophotometer (Shimadzu, UV1201 model). For the measurements, the films were placed in a special film holder of this equipment. The films transparency was determined using the following equation (Cazón et al., 2018):

$$Transparency = \frac{log\%T_{600}}{L} \quad (3)$$

where $\%T_{600}$ is the value of the percentage transmittance at 600 nm (a. u.) and L is the thickness of the film (mm). Three measurements were performed for each film.

2.11. In vitro release of allantoin and zinc ions in simulated wound fluid

The release of bioactive components from the allant-ZnLSH hybrid and the bionanocomposite films was carried out *in vitro* in SWF, prepared as indicated in Section 2.9. The release study from the hybrid material was performed by adding around 10 mg of the solid in several vials with 5 mL of SWF, kept under stirring at 50 rpm in a thermostatic bath (SW23, Julabo) at 35 °C. After different periods, the dispersions were filtered (0.45 μm) and 2 mL of each supernatant were 5-fold diluted and analyzed to determine the released amounts of allantoin and zinc ions. Allantoin content was measured in an Analytik Jena multi N/C 2100 total organic carbon (TOC) analyzer, while the amount of released zinc was determined by total X-ray fluorescence in a TXRF S2 PICOFOX from Bruker.

For the bionanocomposite films, the release of allantoin and zinc was studied using a homemade Franz diffusion cell (Fig. S1 in Supplementary Material). A dialysis membrane (Visking Dialysis Tubing, molecular weight cut-off 12–14,000 Da, from Medicell Membranes Ltd.) was placed between the donor and receptor chambers to simulate the skin. The receptor chamber was filled through the sampling port with 19 mL of SWF and the system was kept at 35 °C and under magnetic stirring. A weighed amount of the bionanocomposite films around 10–20 mg was placed on top of the dialysis membrane in the donor chamber. At different time intervals, an aliquot was taken from the receptor chamber, which was immediately refilled with the same volume of fresh SWF. Finally, the amounts of zinc and allantoin released from each sample were determined by TXRF or TOC analysis, respectively, as indicated above.

2.12. Antibacterial activity assays

The antibacterial activity of the different films containing allant-ZnLSH were evaluated *in vitro* by the disc diffusion method using Mueller-Hinton agar (MHA). For this study, gram-positive bacteria (*Staphylococcus aureus* CECT 239) and gram-negative bacteria (*Escherichia coli* K 12 CECT 433) previously cultured in LB broth (10 g L^{-1} of tryptone, 5 g L^{-1} of yeast extract and 5 g L^{-1} of NaCl) at 36 ± 1 °C for 24 h. Each bacterial dispersion (250 μL, 108 CFU mL^{-1}) was inoculated in MHA and spread with a sterile Drigalski spatula on agar plates prepared at pH 5.5. Discs of 6 mm diameter were cut from selected bionanocomposite films (HPMC, HPMC-9%, HPMC-33%, CMC, CMC-9%, CMC-33%, CNF, CNF-9%, CNF-33%) and, in order to evaluate the properties of the components separately, solutions or dispersions containing each of the tested materials were deposited on similar discs cut from Whatman (W) filters. For this, the hybrid allant-ZnLSH dispersion was deposited on the Whatman filter discs to reach the same proportions as the amounts present in the studied films 9% and 33%, and solutions of $ZnCl_2$ and allantoin were prepared to deposit 5 μL on the Whatman films to have equivalent amounts to those estimated in the studied bionanocomposite discs with 9% and 33% of hybrid: 0.62 mg and 2.27 mg of Zn^{2+}, respectively, and 0.37 mg and 1.35 mg of allantoin, respectively. A positive control with penicillin-streptomycin was used. The prepared samples were placed on previously inoculated agar plates and incubated at 36 ± 1 °C for 24 h.

2.13. Computational methods

Tight binding calculations, which combines reasonable accuracy and computational efficiency, were performed using the DFTB+ code (version 21.2) (Hourahine et al., 2020) on periodic structures. We have used the Slater–Koster parametrization Zn-*X* (*X* = H, C, N, O, S, and Zn) developed by Moreira et al. (2009), also called DFTB/Znorg parametrization, together with the required parameter set of Elstner et al. (1998) (DFTB/mio parametrization). We perform full lattice energy minimization (*i.e.,* relaxing both cell and atomic positions) using the Rational Function Optimizer (RFO) method. DFT-D4 dispersion correction (Caldeweyher et al., 2019) was included by using the Becke–Johnson damping parameters for the Slater–Koster parametrizations of Elstner et al. (1998) of the DFTB Hamiltonian (*i.e.,* $s_6 = 1$, $s_8 = 1.1948145$, $s_9 = 0$, $a_1 = 0.6074567$, and $a_2 = 4.9336133$). The resulting DFTB-D4/Znorg method was used to perform energy minimizations of periodic structures.

We have studied the ketone-enol tautomerism of allantoin with precise methods of functional density theory by Nudged Elastic Band calculations (DFT-NEB). We used the r^2SCAN-3c composite electronic structure method (Grimme et al., 2021), as implemented in the ORCA program (version 5.0.3) (Neese, 2022). For the tautomerism screening of the allantoin molecule (solvated in water) and the molecular optimization calculations we have used the GFN2-xTB basis set as implemented in the xTB (v6.4.0) program package (Bannwarth et al., 2019, 2021). The tautomerism screening was performed by using the CREST (v2.11) program (Pracht et al., 2017, 2020), which uses natively the extended Tight Binding (xTB) method. The implicit water solvation was performed using the ALPB (from Analytical Linearized Poisson–Boltzmann) method (Sigalov et al., 2006). We employed Chemicalize (2022) to identify the most stable tautomer (Major Tautomer) to calculate of the distribution of allantoin species at different pH values.

The insertion of the allantoin anionic species and water molecules into the interlayer was performed using Monte Carlo simulations in the canonical ensemble (NVT MC) using the RASPA code (Dubbeldam et al., 2016). We have used the UFF force field (Rappe et al., 1992).

3. Results and discussion

3.1. Synthesis and characterization of the allantoin-ZnLSH hybrid material

The precipitation of zinc hydroxide in the presence of allantoin following the procedure detailed in the Experimental Section led to the formation of a white solid (allant-ZnLSH). The content of allantoin in

this material was determined by elemental chemical analysis, resulting in 36.8 g per 100 g of allant-ZnLSH hybrid. This method of preparation of the allantoin/zinc hydroxide compound with controlled addition of NaOH provides a more reproducible material and with higher allantoin content than the method described in a patent by Klippel and Margraf (1974), in which the fast addition of NaOH results in materials with variable content in allantoin from one preparation to another. Thus, the materials prepared according to that patented procedure gave an average value of allantoin of 32 ± 3 g/100 g hybrid (RSD = 9.4%), while those obtained with the procedure proposed in the current work gave rise to an average value of 36.8 ± 0.3 g/100 g hybrid (RSD = 0.8%).

The X-ray diffraction pattern of allant-ZnLSH (Fig. 1) confirms the formation of a crystalline solid where no diffraction peaks associated with allantoin crystals are observed. The reflections shown in the diffractogram can be associated with 00l reflections characteristic of a layered structure similar to that of acetate-ZnLSH reported by Poul et al. (2000) and Nyalosaso et al. (2019). From the observed reflections (00*l*) shown in Fig. 1, a basal spacing of 1.808 nm was determined for the allant-ZnLSH hybrid. Taking into account the reported values for the thickness of the ZnLSH layers of 1 nm (Mohsin et al., 2013), the resulting interlayer distance was 0.808 nm. Considering the dimensions of the allantoin molecule, 0.40 × 0.61 nm (Rebitski, 2020), a model can be proposed in which allantoin would intercalate forming a bilayer between the ZnLSH sheets.

The FTIR spectra of allantoin and allant-ZnLSH are collected in Fig. 2. The interaction between Zn and allantoin can be deduced from numerous shifts in the bands in the region from 400 to 1800 cm^{-1}. Among them, the bands observed in the spectrum of allantoin (Fig. 2,a) at 1782 and 1718 cm^{-1}, related to the stretching vibration of C═O in the imidazole ring, or at 1660 cm^{-1}, due to $\nu_{C=O}$ (amide in the ureido group) (Kuş et al., 2009), as well as those attributed to in-plane bending of NH_2 appearing at 1604 cm^{-1}, or to in-plane bending of H-C-N and H-N-C together with C—N stretching in both imidazole and ureido groups observed as several bands at 1532 cm^{-1}, 1433 cm^{-1}, 1401 cm^{-1} and 1361 cm^{-1} (Alam and Ahmad, 2015) are considerably shifted in the spectrum of allant-ZnLSH (Fig. 2,b). The bands at 1326 and 1015 cm^{-1} (in-plane bending and stretching vibrations in the imidazole ring), 1063 cm^{-1} (C-NH_2 stretching vibration and rocking motion of NH_2), 818 cm^{-1} (attributed to C—N and C—C stretching vibration in the imidazole ring) and that at 634 cm^{-1} (associated with ring deformation vibrations) in pure allantoin (Alam and Ahmad, 2015) are also shifted in the spectrum of the hybrid, indicating that the allantoin molecule does not vibrate freely due to its interaction with the inorganic counterpart. In addition, an important change is observed in the region from 3500 to 2750 cm^{-1}, observing only a very broad band centered at 3408 cm^{-1} in the spectrum

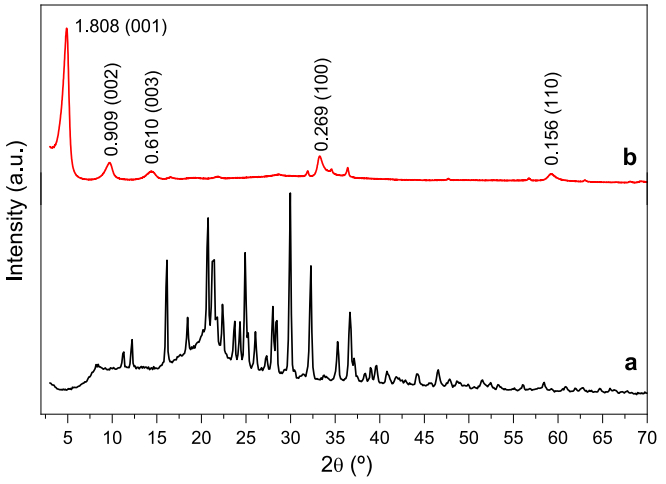

Fig. 1. X-ray diffraction patterns of (a) allantoin and (b) the allant-ZnLSH hybrid material.

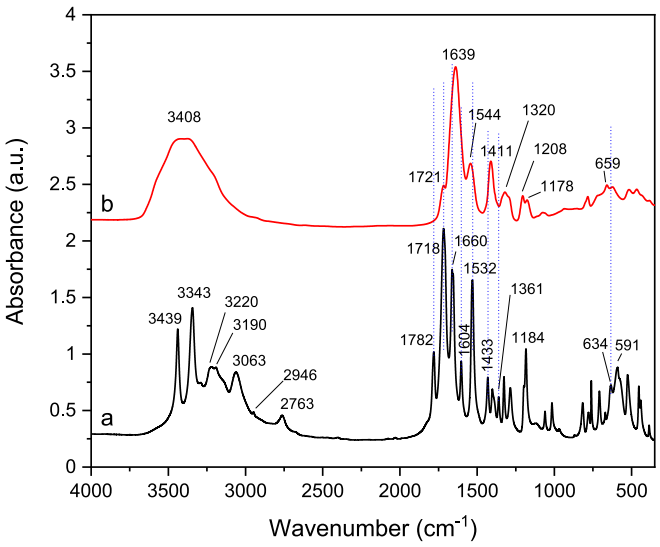

Fig. 2. FTIR spectra in the 4000–350 cm^{-1} wavenumber range of (a) allantoin and (b) the allant-ZnLSH hybrid material.

of the hybrid instead of the clear bands at 3439 and 3343 cm^{-1} attributed to the asymmetric stretching vibration of NH_2 (ν_{as} NH_2) and the NH stretching vibration in the imidazole ring of pristine allantoin, respectively, and the other bands at 3220 and 3190 cm^{-1} assigned to ν_{NH}, or those at 3063 and 2946 cm^{-1} due to ν_{CH} (Kuş et al., 2009). Thus, all these changes would confirm the interaction of allantoin with the Zn hydroxide layers, in agreement with the formation of a LSH where the organic molecule is in direct interaction with Zn substituting a hydroxyl group of the hydroxide structure, as occurs in other systems such as zein-CoLSH (Alcântara et al., 2020). In addition, intermolecular interactions between adjacent allantoin molecules could also take place contributing to the shifts observed in the vibration bands in the FTIR spectrum of the hybrid material.

Solid state NMR spectroscopy can also provide information about the interaction between allantoin and the layered zinc hydroxide. Fig. 3 shows the ^{13}C and ^{15}N spectra of pristine allantoin and the allant-ZnLSH hybrid, which shows the shift of the signals due to carbons 2, 5 and 7 of the carbonyl groups (Rashed et al., 2004) towards higher values, suggesting the participation of these groups in the interaction with the zinc hydroxide. In contrast, the signal attributed to C4 remains nearly

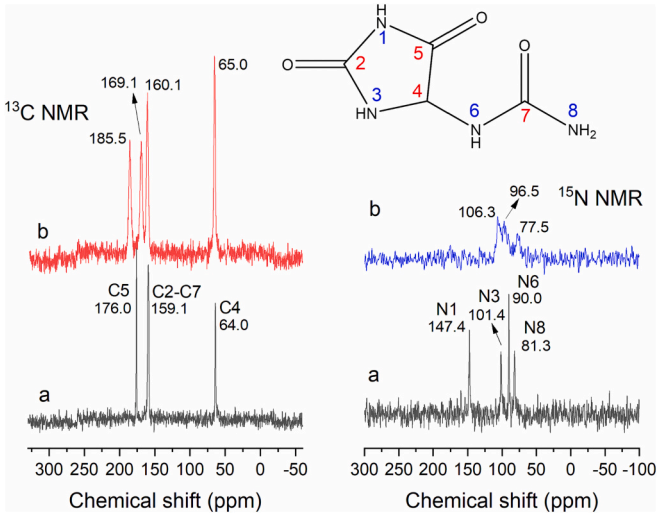

Fig. 3. $^{13}C\{^1H\}$ CP-MAS and $^{15}N\{^1H\}$ CP-MAS NMR spectra of (a) pristine allantoin and (b) the allant-ZnLSH hybrid material.

unaltered at values of 65 ppm, as it would not be involved in the interaction with the LSH. Compared to the ^{13}C NMR spectra of the keto and enol tautomers of allantoin simulated with the ChemBioDraw Ultra 13.0 software (Fig. S2), the bands observed in the experimental ^{13}C NMR spectra shown in Fig. 3 would confirm the higher stability of the keto form. Regarding the ^{15}N NMR spectrum of allantoin, the peak at 147.4 ppm could be assigned to the imide (N1), while that at 101.4 ppm is most likely attributed to the nitrogen from imidazole (N3), and the other two signals at 90.0 and 81.3 ppm could be due to the ureide nitrogens N6 and N8, respectively, according to previous works (Lehmann et al., 2006; Fang et al., 2011). Given that the more perturbed signal in the spectra of allant-ZnLSH is N1, this result would indicate that the interaction with the zinc hydroxide seems to be mainly established through imide nitrogen (N1). The other signals in both NMR spectra show also certain perturbation, which could suggest that coordination of allantoin affects to all the bonds in the molecule, due to interaction with the inorganic layers and intermolecular interaction.

Figure 4 shows the TG/DTA curves of allantoin and the hybrid allant-ZnLSH. The thermal decomposition of allant-ZnLSH shows several consecutive thermal decomposition processes and more differentiated mass losses than in the allantoin profile. The first event occurs at 75 °C and consists of the loss of weakly adsorbed water. Next, the DTA curve of allant-ZnLSH shows an endothermic process at 206 °C that may be related to the elimination of interlayer water and the beginning of the dehydroxylation process (Madej, 2018; Theiss et al., 2013), followed by two exothermic peaks at 477 °C and 549 °C, which may be associated with the breakdown of allantoin together with the dehydroxylation of the LSH. As expected, the hybrid material shows the decomposition of allantoin associated with the zinc hydroxide starting at higher temperature and lasting until 50 °C above. At the end of the process, around 50% of the starting mass is lost in contrast to pristine allantoin, which is completely decomposed. This is due to the presence of zinc oxides formed during the thermal process. Taking into account that the water content in the hybrid material was 6.5 g per 100 g of hybrid, determined from TG, the elemental chemical analysis provided a value of 36.8 g of allantoin per 100 g of hybrid, and the allantoin/Zn ratio determined by EDX is 0.38, the following formula can be proposed: $Zn_2(OH)_{3.24}(allant)_{0.76}{\cdot}1.18H_2O$.

Figure 5 shows several SEM images of the allant-ZnLSH hybrid that reveal the presence of a fairly homogeneous solid, whose particles appear to have a lamellar morphology and are arranged in the shape of a desert rose, a typical structure of various layered hydroxides. TEM images (Fig. S3) show the hybrid is actually formed by particles of around 200 nm diameter, showing an irregular shape. The EDX analyses of the

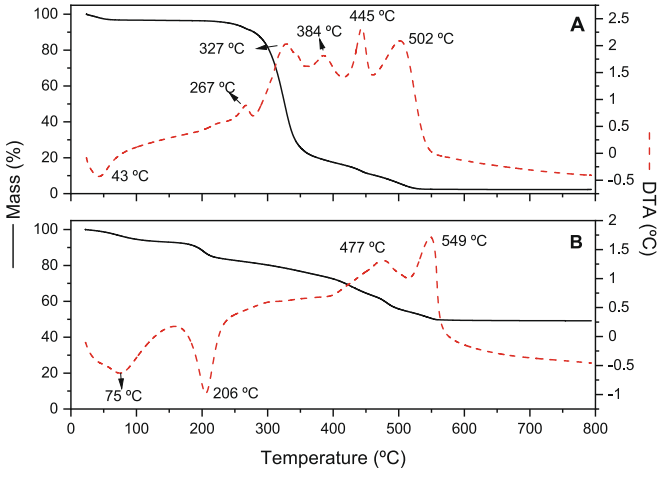

Fig. 4. Thermogravimetric analysis and differential thermal analysis of (A) pristine allantoin and (B) the allant-ZnLSH hybrid material, from room temperature to 800 °C at a heating rate of 10 °C/min under air flow (100 mL/min).

content of C, N and Zn throughout the solid confirmed a homogeneous distribution of the elements, resulting in the following average %wt values from four measurements: C: 19.2%, N: 13.8% and Zn: 42.7%. The %wt values for Zn and N match well with the theoretical values estimated from the proposed composition, but the %C measured with EDX can be inaccurate due to the carbon detected from the carbon tape used to stick the samples to the aluminum holder.

3.2. Structure prediction and computational results

Firstly, we have performed an analysis of the distribution of anionic species of allantoin under different pH conditions. We also consider keto-enol tautomerism; however, we obtained that the enol form is slightly more unstable than the ketone enantiomeric forms, as observed by performing NEB calculations (see Fig. S4 in Supplementary Material for more details). In Fig. 6 we show the distribution of species at different pH. The strongest acidic, the NH between the two ketone groups, has a pKa of 7.95. The most common tautomer species are, in increasing order of medium pH: 1, 2, 4, and 8, with 0, −1, −2, and − 3 formal charges, respectively. The other species are found with a frequency of <5%. Then, we optimized the molecular structure of the allantoin species (1, 2, 4, and 8 of Fig. 6), and the water molecule at DFTB-D4/Znorg theoretical level.

Secondly, we have constructed the allant-ZnLSH hybrid complex. We started from the Zn and O positions of the refined X-ray structure for $Zn_5(OH)_{10}{\cdot}2H_2O$ reported by Gordeeva et al. (2020), to which H atoms were added. This periodic structure was optimized by energy minimization methods at the same theoretical level than with allantoin species. The cell parameters of the Zn-LSH predicted by the DFTB-D4/Znorg theoretical level are in good agreement with the predicted cell parameters by Gordeeva et al. (2020). These results confirm that the thickness of the ZnLSH layers cannot be considered to be 1 nm, as indicated in Section 3.1, but the value deduced in the current case is 0.764 nm (see Fig. 7).

Once the Zn-LSH films were optimized, we removed the central LSH slice (see Fig. 7), increased the lattice parameter to 2 nm, and removed the four OH^- anions bonded to the tetrahedral Zn and the water molecules. Then, using Markov Chain Monte Carlo (MCMC) simulations in the canonical ensemble (NVT), we inserted four (*R*)-(−)-allantoin anions (−1 point charge) per unit cell by keeping the heterocycles as close to the tetrahedral Zn atoms. After performing 200,000 MCNVT steps, we ran five cycles of MD simulations in the NVT ensemble using the DFTB-D4/Znorg method with a temperature ramp from 200 to 400 K at 100 ps per cycle. We then inserted 6, 8, 9, and 10 water molecules by repeating the procedure used for the allantoin anion, and then performed an annealing process in the isothermal-isobaric ensemble (NPT) to obtain the final structures. In this way, we obtain a material with the composition: $Zn(OH)_{1.6}((R)\text{-allant})_{0.4}{\cdot}w\ H_2O$, with w = 0.6, 0.8, 0.9, and 1, respectively. In the NPT MD simulations, the most common microstates are those in which the allantoin anion is observed to bind to the tetrahedral Zn *via* the N1 atom. However, during MD, we observed occasional interactions between the C=O groups of allantoin and the neighboring Zn. The corresponding formation energies with respect to the Zn-LSH material, the solvated allantoin and n water molecules (*i.e.,* $2\,(Zn_5(OH)_{10}) + n\,H_2O + 4\,(allant)^- \rightarrow Zn_{10}(OH)_{16}(allant)_4^-{\cdot}(n+4)\,H_2O$), are: −0.639, −0.661, −0.659, and − 0.645 eV per Zn atom, for n = 2, 4, 5, and 6, respectively. Therefore, the simulation predicts a slightly higher amount of water than calculated from TG, see Fig. 4, (w = 0.8 *versus* 0.6, respectively). For n = 4 (w = 0.8, the more stable composition), the resulting enantiopure (*R*)-(−)-allant-Zn-LSH has a basal distance and an interlayer distance of 1.802 nm and 1.038 nm, respectively (Fig. 8). The interlayer distance was calculated by subtracting the basal distance of the Zn-LSH material (0.764 nm, see Fig. 7) to the basal distance of the hybrid material (1.802 nm, see Fig. 8), which is in agreement with that obtained by X-ray diffraction.

In the synthesis process, we used a racemic mixture of allantoin.

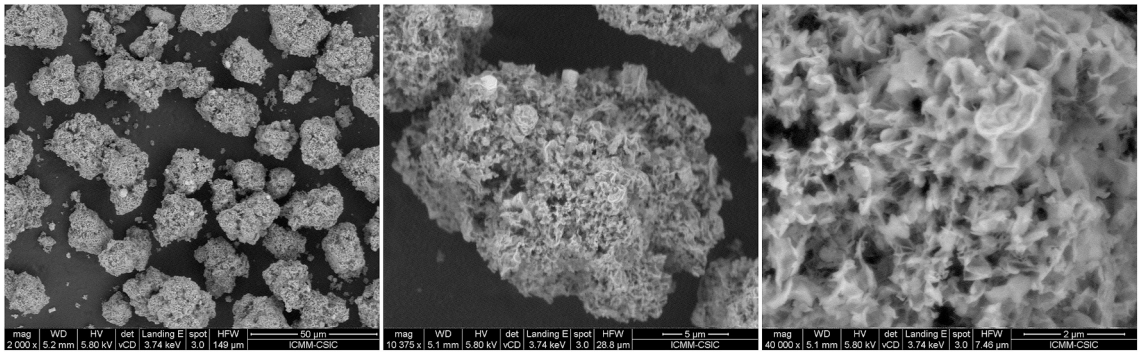

Fig. 5. FESEM images of the allant-ZnLSH hybrid at different magnification.

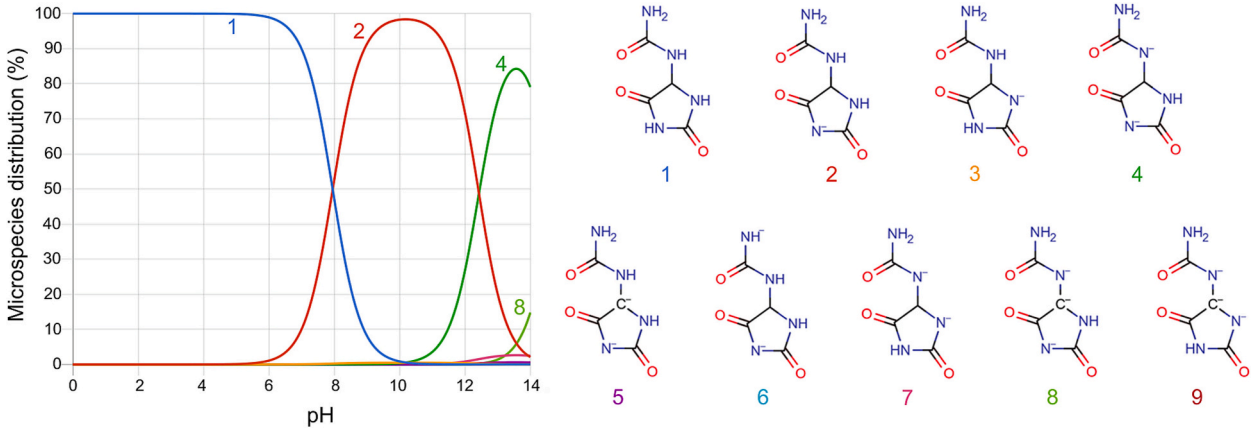

Fig. 6. Species distribution of the allantoin molecule at different pH values. Three species, with charge 0, −1, and − 2 are dominant over the whole range of pH values.

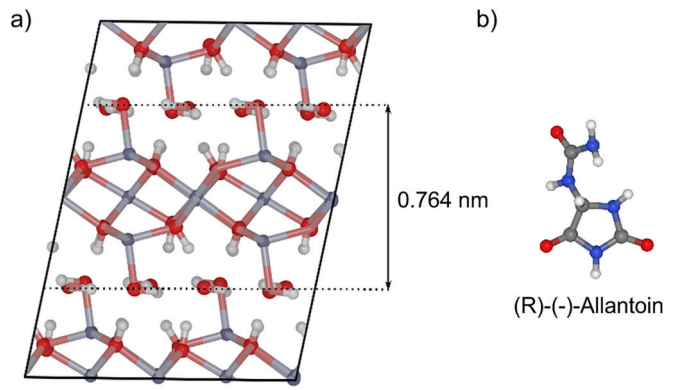

Fig. 7. Snapshot of the a) optimized Zn-LSH material (2 × 1 × 1 supercell), and b) optimized molecular structure of the more stable solvated (*R*)-(−)-allantoin conformer. The basal distance of the optimized structure is marked between the dotted lines (0.764 nm).

Consequently, we also studied the structural stability considering some representative mixtures of the enantiomers of allantoin. Once the structure with eight water molecules and four (R)-allantoin molecules per unit cell (4R) was optimized we have obtained the mixing-enantiomer structures: (3R, S), (2R, 2S), (R, 3S) and (4S). To construct the structures we exchanged one, two, three, and four (R)-allantoin molecules for their corresponding (S)-enantiomer, and optimized the periodic systems (atom positions and cell parameters) again, previously carrying out an annealing process (MD NPT from 300 to 350 K, and from 350 to 300 K, 50 ps each simulation). This method leads to differences energies of −3.86, −4.42, 10.25 and 12.67 kcal mol^{-1}, for the (3R, S), (2R, 2S), (R, 3S), and (4S) structures, respectively, having as reference the energy of the pure (4R) structure. Therefore, the racemic composition is the most stable polymorph, but high-enantiomeric purity crystals (4R per unit cell) cannot be discarded. However, further dedicated studies, considering larger supercells and site order disorder, are necessary to have a complete view of the phenomena, which is outside the main scope of this work. The optimized structure with racemic mixture exhibits a basal distance and an interlayer space of 1.68 nm and 0.91 nm, respectively. In addition, we observed positive thermal expansion in the NPT MD simulations (mainly in the perpendicular direction of the interlayer), so the expected value of interlayer distance is slightly larger (*ca.* 0.97 nm) at 300 K.

3.3. *Preparation of bionanocomposite films incorporating the allantoin-ZnLSH hybrid*

Several cellulosic materials were evaluated for the preparation of bionanocomposite films incorporating the nanoparticles of allant-ZnLSH hybrid for potential application as wound dressings. Cellulose derivatives such as hydroxypropylmethylcellulose (HPMC) and carboxymethylcellulose (CMC) as well as cellulose nanofibers (CNF) were chosen because of their biocompatibility, biodegradability, and good film forming ability suitable for wound healing applications (Amalraj et al., 2018; Dharmalingam and Anandalakshmi, 2019; Kanikireddy et al., 2020), incorporating different amounts of allant-ZnLSH as indicated in Table 1. The resulting films (Fig. 9) show a uniform appearance, indicating a homogeneous distribution of the hybrid particles. This is advantageous in order to have an even distribution of allantoin in the materials, given the difficulty of preparing biopolymer films by direct

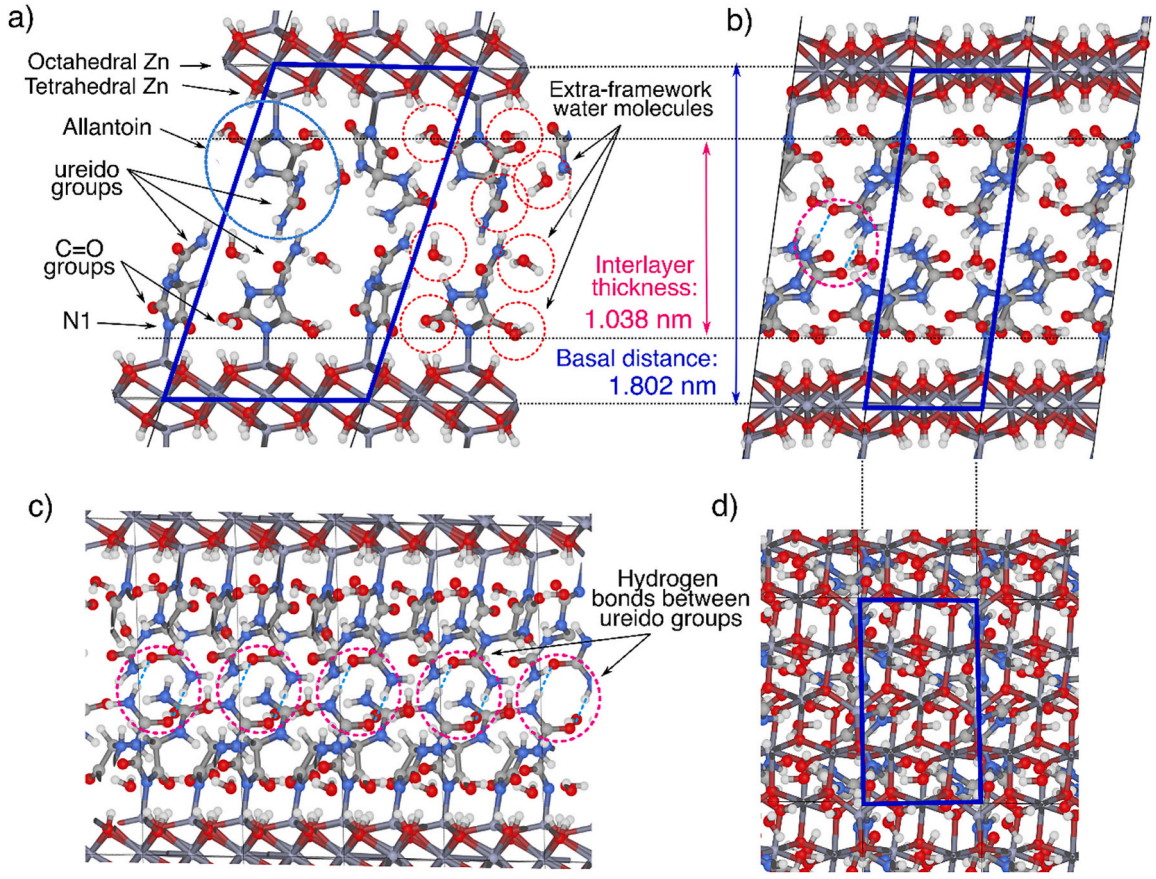

Fig. 8. Four snapshots of the proposed model for the LSH-(*R*)-allantoin hybrid material with composition $Zn(OH)_{1.6}((R)\text{-allant})_{0.4}$ 0.8 H_2O for: a) 100-view, b) 010-view, c) 110-view, and d) 001-view. The unit cell box is indicated in thick blue lines. We have indicated in this figure the relevant atoms and groups of allantoin for the structural description of the material. In the c) panel we indicated the formation of two single NH···O=COH H-bonds between the ureido group of the allantoin molecules of different layers. We have also indicated the basal distance and the thickness of the interlayer. (For interpretation of the references to colour in this figure legend, the reader is referred to the web version of this article.)

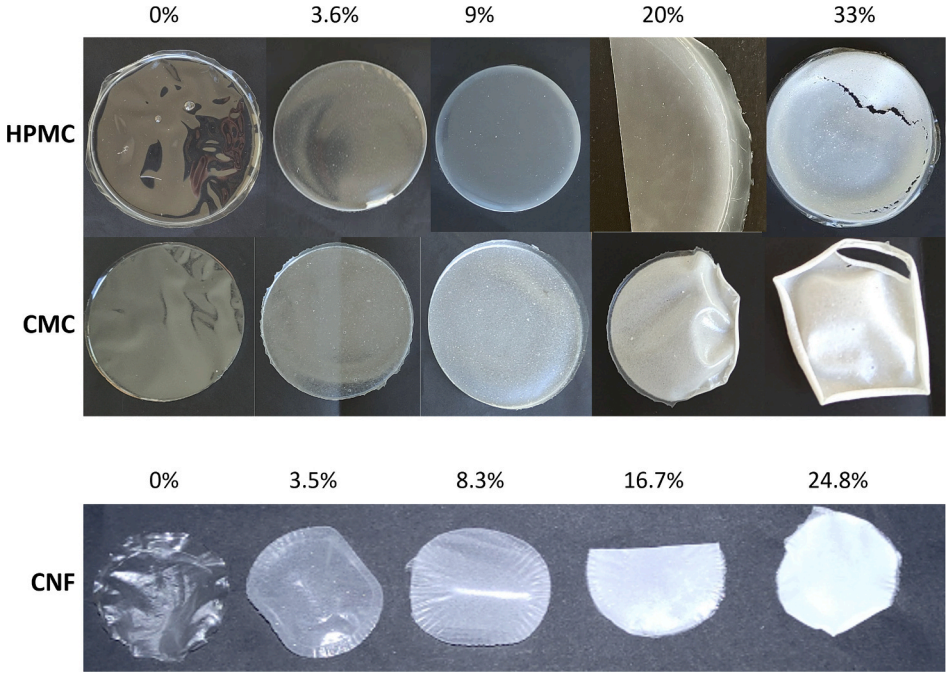

Fig. 9. Appearance of the HPMC, CMC and CNF films with the incorporation of the hybrid at different proportions.

incorporation of this molecule, which results in inhomogeneous materials with large agglomerates of allantoin due to the low solubility of this molecule (Fig. S5). It was confirmed by XRD that the resulting bionanocomposites consisted in the hybrid nanoparticles dispersed within the biopolymer matrix, with no intercalation of the polymer between the inorganic layers (Fig. S6).

The mechanical properties of the bionanocomposite films were evaluated by means of a universal mechanical test machine. Tensile testing resulted in the values of Young's modulus and the percentage of elongation at break collected in Table 2. The Young's modulus values obtained in the tests show a similar trend in the three groups of materials, slightly increasing as the hybrid loading rises up to 9%. The highest value, 3.9 GPa, is obtained for the CMC-9% film. In all cases, when the hybrid loading is higher than 9%, a slight decrease is produced in Young's modulus, but these films still show close values in all the studied systems. As observed for other reinforced polysaccharides (Darder et al., 2021; González del Campo et al., 2018), the values of elongation at break decrease as the hybrid loading increases, reaching extremely low values around 1% in the case of HPMC and CMC materials with 33% hybrid loading, which indicates that these films are quite brittle. However, for CNF films, the percentage of elongation at break is higher (>5%) even for the CNF-33% film, which indicates the greater flexibility of these films compared to those of HPMC and CMC. This may be due to the fact that the CNF structure consists of intertwined nanofibers and is not a compact polymeric structure as occurs in the case of HPMC and CMC matrices. According to the results of the tensile testing, the optimal films would be those with around 9% of hybrid in its composition, as higher amounts slightly decrease the mechanical properties leading to brittle films. However, to reach a compromise in order to have the best possible antimicrobial activity (as shown below) while keeping appropriate mechanical resistance to handling, and therefore the films containing 20% of hybrid were characterized as well.

The aspect of the films varies from the pure polymers to those incorporating the hybrid. For instance, Fig. S7 shows FESEM images of the surface of HPMC, CMC, and CNF films without and with 9% *w*/w of allant-ZnLSH, where the presence of particles can be observed even if they are integrated within the polymer matrices. Fig. 10 shows the cross-sectional and surface FESEM images on the smooth side (dried in contact with the petri dish) and on the rough side (air dried) of the films with 9% hybrid loading. The images of HPMC- and CMC-based films show a similar morphology between both faces of the film and the presence of aggregates of small particles that correspond to the allant-ZnLSH hybrid. In the CNF films, the nanocellulose fibers are not distinguished, but the existence of aggregates of particles on the surface is appreciated. On the other hand, cross-sectional images reveal a compact structure inside the film. In the case of HPMC- and CNF-based films, agglomerates of particles homogeneously distributed throughout the film can be observed. However, the CMC-based film shows a compact and homogeneous structure where aggregates of particles are hardly distinguished.

Table 2
Values of Young's modulus (E) and elongation at break (EB) obtained for the bionanocomposite films.

	HPMC		CMC			CNF	
Amount of hybrid (% *w*/w)	E (GPa)	EB (%)	E (GPa)	EB (%)	Amount of hybrid (% w/w)	E (GPa)	EB (%)
0	1.7 ± 0.4	23.8 ± 5.5	2.8 ± 0.4	6.5 ± 0.2	0	2.1 ± 0.1	7.2 ± 2.6
3.6	2.0 ± 0.2	12.7 ± 1.6	3.8 ± 0.4	3.8 ± 0.9	3.5	2.6 ± 0.2	5.6 ± 2.4
9.0	2.1 ± 0.1	5.3 ± 0.6	3.9 ± 0.3	3.2 ± 0.1	8.3	3.30 ± 0.03	4.0 ± 0.5
20.0	1.8 ± 0.2	2.6 ± 1.0	3.3 ± 0.1	2.4 ± 0.7	16.7	1.3 ± 0.5	11.6 ± 2.1
33.0	1.8 ± 0.3	1.0 ± 0.2	3.5 ± 0.5	1.4 ± 0.4	24.8	1.50 ± 0.03	5.3 ± 1.9

In order to study the capacity of the films to adsorb water under certain humidity and temperature conditions, the water adsorption isotherms were obtained at 27 °C for these selected films: pristine polymers without incorporation of the hybrid (0%), and films with 9% and 20% hybrid loading for comparison. As can be seen in Fig. 11, all the films adsorb a low amount of water up to 50% relative humidity, which is especially low in the case of CMC, whose isotherms show that practically no water is retained up to RH values of 30%. However, the CMC-based films present a more hygroscopic character at higher humidity values, most likely due to the carboxymethyl groups in its structure. At higher values of relative humidity, the formation of water clusters occurs on the surface of the films leading to large amounts of adsorbed water, a behavior that is observed in the final zone of the isotherms from around 70 to 95% RH. In the HPMC- and CNF-based films, the incorporation of allant-ZnLSH does not produce a significant change in the amount of adsorbed water, and only slight variations can be observed at the highest RH values. In the CMC-based films the addition of 9% *w/w* does not alter the water uptake, but higher amounts of hybrid loading produce a reduction in amount of adsorbed water even at RH 30% and higher. These results confirm that the water adsorption of these biopolymers is not impaired by the addition of the allant-ZnLSH hybrid in amounts around 9%, which were considered optimal according to their best mechanical properties as indicated above. A similar behavior was observed in HPMC-based bionanocomposite films where the presence of gentamicin-montmorillonite did not alter the water uptake of the biopolymer (Darder et al., 2021).

The ability to absorb wound exudates is also of great interest for the application of biopolymeric materials as wound dressings (Jin et al., 2016). For this purpose, the water absorption capacity of the bionanocomposite films containing 20% of allant-ZnLSH hybrid was determined in simulated wound fluid. The HPMC and CMC films in contact with SWF solution swelled resulting into a hydrogel. CMC films were able to retain their original shape but with higher dimensions, while the HPMC material lost its conformation resulting in a viscous gel and it was difficult to recover from the SWF. For the CMC-based material, a WAC of around 5000% was estimated although it was difficult to carry out a precise measurement. In contrast, the CNF films underwent swelling preserving their original shape, and they were able to absorb a large amount of water giving a WAC value of 318 ± 6%. These results are in the range of those reported for analogous biopolymer-based dressings (Dharmalingam and Anandalakshmi, 2019; Mi et al., 2001), indicating the suitability of the developed bionanocomposite materials for this application.

The permeability of dressings to water vapor is also of interest for wound healing purposes, as they should maintain a suitable level of moisture and prevent wound dehydration in order to favor the healing process (Gonzalez et al., 2014; Mi et al., 2001; Xu et al., 2016). The transmission of water vapor through the bionanocomposite films was evaluated for the films with 0, 9% w/w and 20% w/w of allant-ZnLSH following the procedure described in the Experimental Section. The representation of the mass of water gained as a function of time made it possible to obtain the water vapor transmission rate (WVTR) for each film studied (Fig. S8). Table 3 shows the determined WVTR values, as well as the water vapor permeability (WVP) values calculated from them using eq. (1). Although the WVTR values vary slightly after the addition of the hybrid, these changes are not significant taking into account the standard deviation values. Thus, these results confirm that the addition of allant-ZnLSH does not perturb considerably the WVTR of the pristine biopolymer films, similar to what was observed in the moisture adsorption study. The determined WVTR values are in the range of values estimated for injured skin, which are reported to vary between

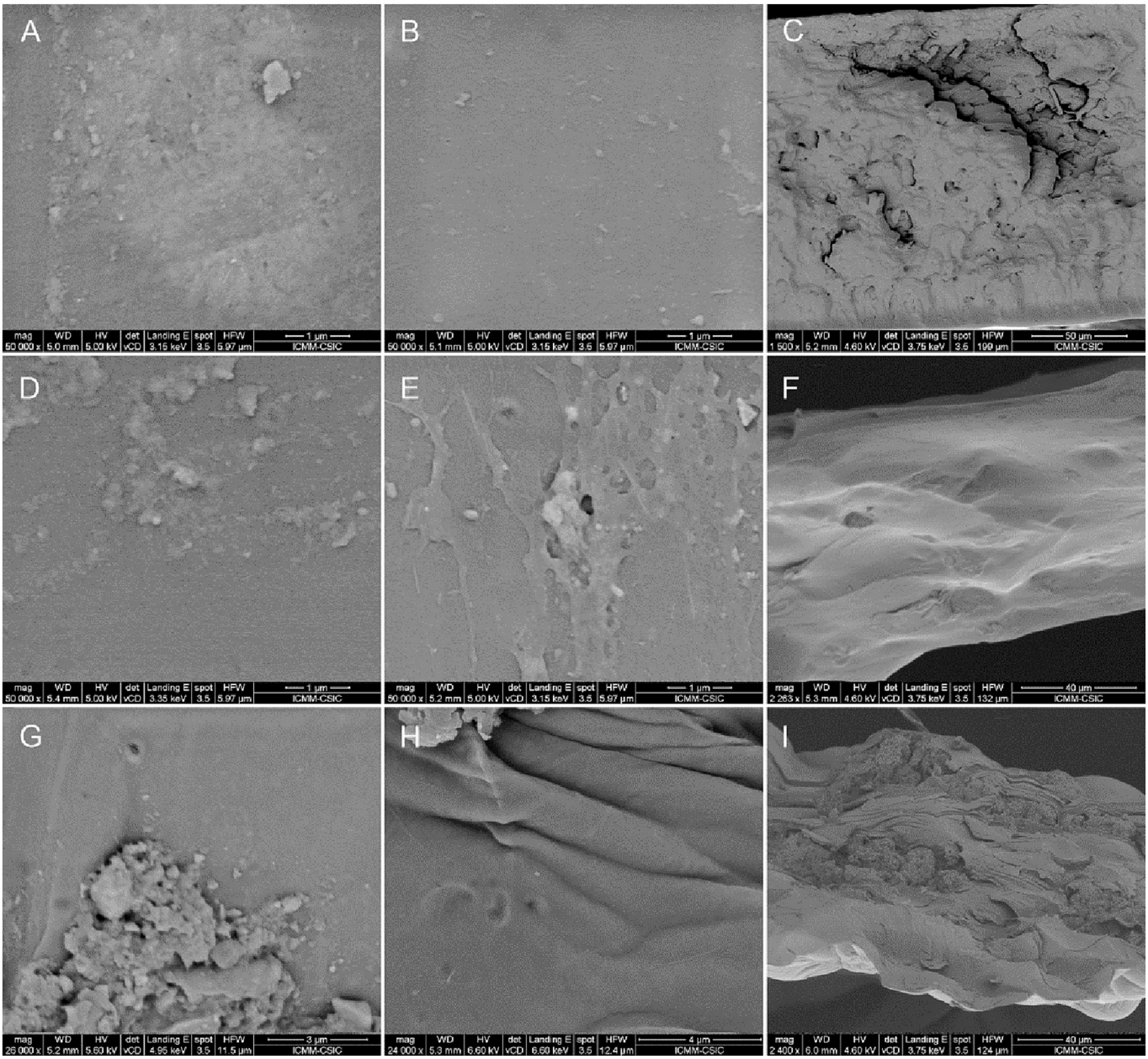

Fig. 10. Surface and cross-sectional images of (A-C) HPMC, (D—F) CMC, and (G-I) CNF films loaded with 9% *w*/w of allant-ZnLSH, showing (A,D,G) the upper face, (B,E,H) the lower face and (C,F,I) a cross section.

264 and 4800 g/m^2 day, while the value determined for normal skin is 204 g/m^2 day (Gonzalez et al., 2014). Although WVTR values around 2000–2500 g/m^2 day were reported as optimal for application in wound healing (Mi et al., 2001; Xu et al., 2016), tested films with lower values between 50 and 950 g/m^2 day have also proven suitable to control water loss and promote cell growth (Xu et al., 2016). The WVTR values were used to calculate the WVP of each material, which are also collected in Table 3.

Visible light transparent films can be very convenient when used as wound dressing to monitor the progress of wound healing without the need to remove the dressing (Di et al., 2017; Vowden and Vowden, 2017). Another interesting characteristic is the possibility of preventing the passage of UV light to afford greater protection of wounds against UV radiation (Cunha et al., 2020). Fig. 12 shows the transmittance curves in the 200–800 nm region of the UV–Vis spectrum for the different biopolymer films and bionanocomposites with 9% and 20% hybrid loadings, and Table 4 summarizes the transmittance percentage and transparency values at 600 nm for the different films and their compositions. The three biopolymer films present high transmittance values around 90% in the visible region of the spectrum, while a reduction in the transmittance percentage is observed as the hybrid loading increases, as indicated in Table 4. However, the bionanocomposite films containing allant-ZnLSH still show an acceptable degree of transparency, which would be advantageous to monitor the evolution of the wound. Below 400 nm, all of the systems show a certain decrease in %T, mainly in the case of films with the highest amount of hybrid, which would indicate that the dispersed hybrid provides barrier properties to the passage of UV light, as reported for other cellulose-clay materials (Alcantara et al., 2016; Martín-Sampedro et al., 2022).

3.4. Release of zinc and allantoin from the bionanocomposite films and evaluation of the antimicrobial activity

Allantoin and zinc release studies were carried out for the allant-

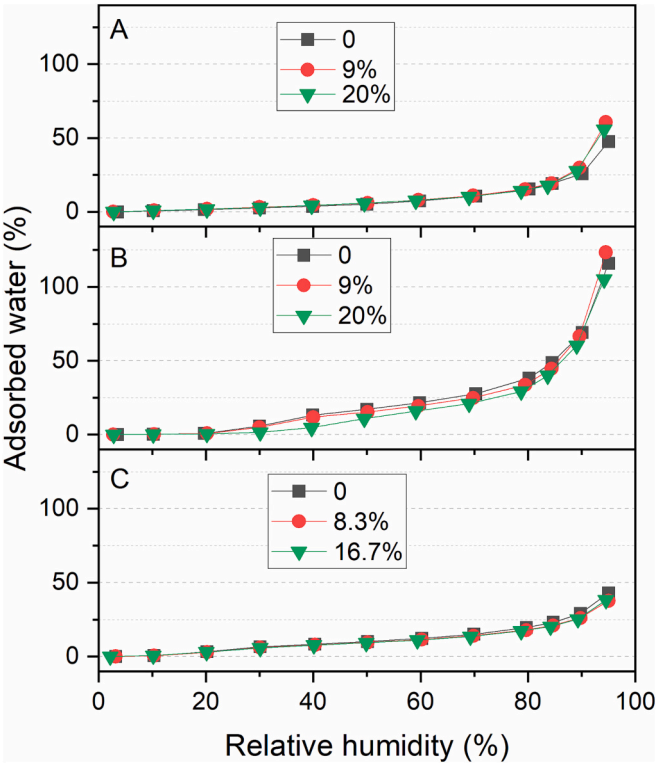

Fig. 11. Water adsorption isotherms for (A) HPMC, (B) CMC, and (C) CNF bionanocomposite films in the relative humidity range from 0 to 95%, at 27 °C.

Table 3
WVTR and WVP values of the biopolymer films and the bionanocomposite films with a hybrid amount of 9% w/w.

	Amount of hybrid (% w/w)	WVTR (g/m^2 day)	WVP (g/Pa s m) × 10^{10}
HPMC	0	342 ± 21	2.0 ± 0.1
	9	260 ± 176	1.7 ± 1.2
	20	256 ± 94	2.3 ± 0.9
CMC	0	540 ± 227	3.0 ± 1.3
	9	424 ± 174	2.4 ± 1.0
	20	474 ± 7	3.70 ± 0.05
CNF	0	568 ± 9	0.90 ± 0.01
	8.3	633 ± 182	1.2 ± 0.4
	16.7	580 ± 55	1.3 ± 0.1

ZnLSH hybrid as well as for the bionanocomposite films with a hybrid loading of 20%wt (or 16.7% in the CNF-based material). The kinetics of allantoin and zinc release from the hybrid material were evaluated in simulated wound fluid (SWF) solution in a thermostatic shaker at 35 °C for 7 days, determining the amounts of allantoin (from TOC measurements) and Zn^{2+} (from TXRF measurements) released at different times (Fig. 13A). A rapid release of allantoin is observed within the first 4 h, which can be due to exchange of allantoin molecules by the chloride anions present in SWF, and then the release rate is reduced leading to a gradual liberation of allantoin during the following days. Similarly, the release profile of zinc cations shows different liberation rates at different stages of the study, maintaining a sustained release for several days. As confirmed by XRD (Fig. S6), the structure of the allant-ZnLSH material is preserved in spite of the Zn release determined after several hours in SWF.

The release of zinc cations and allantoin from the bionanocomposite films was evaluated in SWF using a homemade Franz diffusion cell (Fig. S1). As can be seen in Fig. 13B, the released allantoin values determined in the receptor chamber after 24 were close to 84% for the HPMC-20% film, while the released values for the CMC- and CNF-based materials are around 64% and 68%, respectively. These results could be attributed to the different swelling degree of these films as discussed above, as the HPMC material showed a large adsorption of water resulting in a gel, while the other materials preserved their conformation. However, the behavior is different regarding the release of Zn^{2+} (Fig. 13C), since the largest amount is determined for the CNF-16.7% film. This fact could be attributed to the nature of the CNF film formed by intertwined fibers. In this case, diffusion can be faster than in HPMC and CMC bulky nanocomposite materials that undergo an important swelling effect in contact with water, leading to a dense and viscous gel where the zinc cations can remain trapped near the net charges. In all cases, the measured values of zinc and allantoin are higher than those released from the allant-LSH hybrid after 24 h, around 35% allantoin and 0.88% Zn^{2+}. This fact could be attributed to a partial release during the dispersion of the hybrid in the biopolymers solutions and the subsequent conformation of the bionanocomposite films. The release kinetics of zinc and allantoin were determined for the HPMC-20% film using the diffusion cell, showing a gradual release of both components over several days (Fig. S9), which confirms the ability of this type of bionanocomposite films to provide an antimicrobial agent when used as a wound dressing.

The antimicrobial properties of the cellulosic films containing allant-ZnLSH were evaluated against *E. coli* and *S. aureus* bacteria using the disc diffusion method after 24 h of incubation at 37 °C. Any of the materials analyzed in the agar plates with *E. coli* showed an inhibition halo, being the antimicrobial activity only determined for some of the bionanocomposite films against *S. aureus* (Fig. 14). The measured

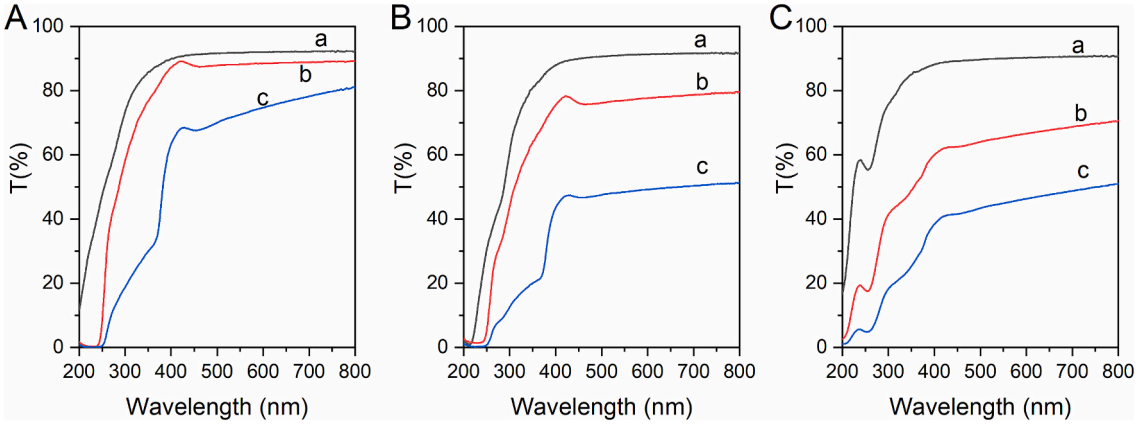

Fig. 12. Variation of light transmittance between 800 and 200 nm of the (A) HPMC, (B) CMC, and (C) CNF films containing (a) 0%, (b) 9% and (c) 20% allant-ZnLSH in the HPMC- and CMC-based films, and (a) 0%, (b) 8.3% and (c) 16.7% allant-ZnLSH in the CNF-based films.

Table 4
Transmittance percentage and transparency values at 600 nm for bionanocomposite films compared to the pristine biopolymers.

	HPMC		CMC			CNF	
Amount of hybrid (% w/w)	$\%T_{600}$ (a.u.)	Transparency (a.u./mm)	$\%T_{600}$ (a.u.)	Transparency (a.u./mm)	Amount of hybrid (% w/w)	$\%T_{600}$ (a.u.)	Transparency (a.u./mm)
0%	92.1	16.3	91.3	16.9	**0%**	90.3	60.0
9%	88.5	14.5	77.7	16.2	**8.3%**	66.6	46.0
20%	74.7	15.4	49.2	10.6	**16.7%**	46.3	36.4

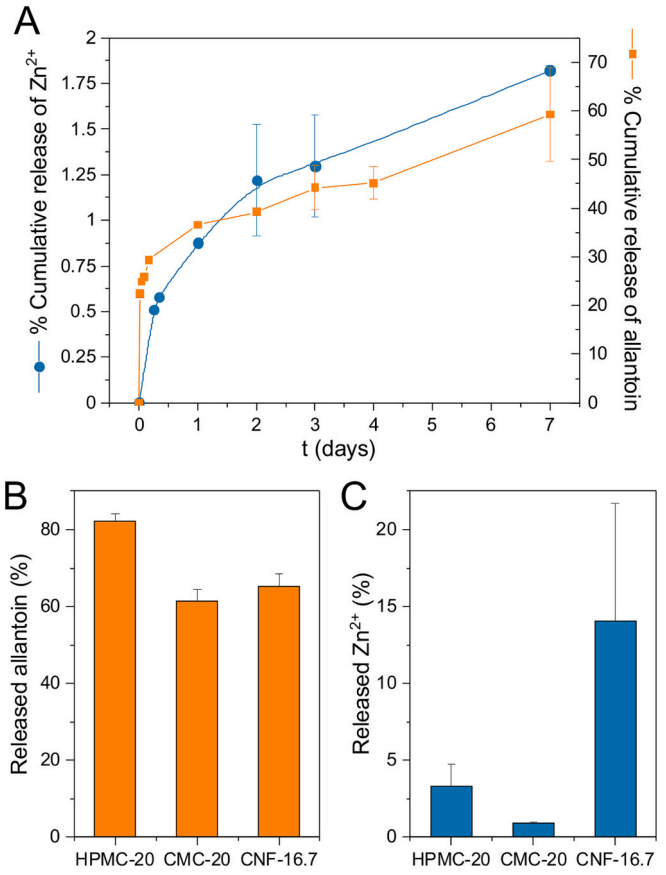

Fig. 13. (A) Release kinetics of zinc and allantoin from the allant-ZnLSH hybrid in SWF in a thermostatic shaker at 35 °C. Release of (B) allantoin and (C) zinc after 24 h from the films HPMC-20%, CMC-20%, and CNF-16.7% using the Franz diffusion cell with SWF at 35 °C.

diameter of the inhibition halos are collected in Table S1. As shown in Fig. 14 for *S. aureus* tests, the pristine biopolymer films without hybrid (samples 1, 4 and 7) do not show any inhibition halo. The same result is observed for the Whatman disc supporting allantoin, confirming that this biomolecule does not show bactericidal properties, at least at the studied concentration. Antimicrobial activity was clearly observed in bionanocomposites based on HPMC and CNF, with a clearer halo in discs with the highest amount of hybrid, as well as for the Whatman filter discs loaded with Zn^{2+} and the allant-ZnLSH hybrid. In the case of CNF-24.8% films (sample 9), the inhibition halo is slightly smaller than that observed for the HPMC-33% film, which can be due to the lower amount of hybrid loaded in the CNF films. In the case of CMC bionanocomposite films, small or none inhibition halos can be seen, indicating a low release of Zn^{2+}, (samples 5 and 6), which could be due to the smaller release of Zn^{2+} from the CMC-based film, as shown in Fig. 13C. This fact could be attributed to the electrostatic retention of zinc cations by the negatively charged chains of this polysaccharide. These results reveal how the chosen biopolymeric matrix can modify the release capacity of Zn^{2+} into the medium. A detailed study for all the prepared compositions is shown in Fig. S10, confirming that bionanocomposite films loaded with 20% of hybrid, or 16.7% in the case of CNF, provide antibacterial activity while showing better mechanical properties than films with the highest hybrid content.

The activity of these materials against *S. aureus* is related to the presence of Zn^{2+}, which is known to be more effective against Gram-positive bacteria (Siddiqi et al., 2018). In fact, large inhibition halos are observed against *S. aureus* around the Whatman filter discs containing $ZnCl_2$ (samples 10 and 11) in equivalent amounts to the Zn^{2+} content of the bionanocomposite films with 9% and 33% hybrid, respectively. However, the larger diameter of the halos around discs 10 and 11 may be due to the fact that the ions are released directly into the medium from dissolved $ZnCl_2$, while in the bionanocomposite films Zn^{2+} ions form part of the LSH structure and are released more slowly. In fact, when the allant-ZnLSH hybrid is deposited on a Whatman filter (samples 12 and 13), the halos observed around these discs have a similar size than those appearing around the HPMC- and CNF-based bionanocomposite films. These results show the antimicrobial activity of cellulosic films loaded with allant-ZnLSH against *S. aureus*, one of the main causes of skin infections in humans and animals, and their suitable mechanical and optical properties and water permeability support their potential use as antimicrobial dressings for the healing of injured skin.

4. Conclusions

In the present study, bionanocomposite films based on cellulosic derivatives (hydroxypropylmethylcellulose, carboxymethylcellulose and nanofibrillated cellulose) were prepared by incorporation of a zinc layered simple hydroxide (ZnLSH) that contains allantoin, in order to confer antimicrobial and skin regenerative properties to the resulting films, which could be potentially applied as wound dressings. The allantoin-ZnLSH hybrid was prepared by coprecipitation of the zinc hydroxide in the presence of allantoin under controlled pH, which resulted in 58.6 g of adsorbed allantoin per 100 g of ZnLSH. With the results obtained by elemental chemical analysis, TG and EDX, the formula deduced for the hybrid was $Zn_2(OH)_{3.24}(allant)_{0.76}{\cdot}1.18H_2O$. X-ray diffraction confirmed the formation of a lamellar structure in which allantoin could be arranged in the form of a bilayer. FTIR and ^{13}C and ^{15}N solid state NMR spectroscopies confirmed the interactions established between Zn^{2+} ions and the carbonyl and N-containing groups of allantoin. Computational studies are in agreement with the experimental data, confirming the intercalation of allantoin as a bilayer and the interaction of the allantoin molecule through the heterocycle, mainly involving the imide nitrogen.

The HPMC-, CMC- and CNF-based bionanocomposites were prepared by incorporation of increasing amounts of the allant-ZnLSH hybrid. The films exhibited good mechanical properties, being the best results of resistance and elasticity obtained for that containing 9% of hybrid. The films showed also suitable water vapor transmission rate, in the range of values reported for other wound dressings, as well as an acceptable degree of transparency to allow monitoring the evolution of the wound without removing the dressing. The values obtained in the release studies of zinc and allantoin from the hybrid indicate that a gradual release of both components is maintained for several days. Release studies from the bionanocomposite films carried out in a diffusion cell

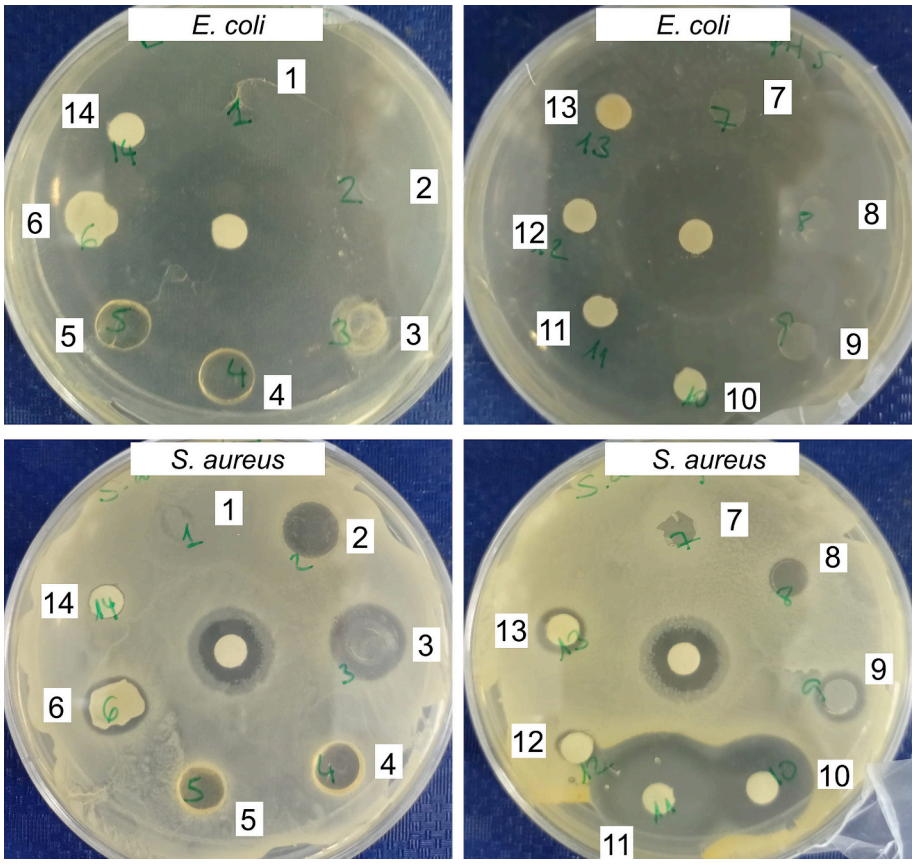

Fig. 14. Images showing the evolution of the growth of the microbial population after 24 h of the colonies of *E. coli* and *S. aureus* around discs of the following materials: 1) HPMC, 2) HPMC-9%, 3) HPMC-33%, 4) CMC, 5) CMC-9%, 6) CMC-33%, 7) CNF, 8) CNF-8.3%, and 9) CNF-24.8%; and Whatman filter discs supporting 10) Zn^{2+} 0.34 mg, 11) Zn^{2+} 1.27 mg, 12) allant-ZnLSH 0.62 mg, 13) allant-ZnLSH 2.27 mg, and 14) allantoin 1.35 mg. A positive control with penicillin-streptomycin was placed in the center of each plate.

also showed the gradual release of both components for several days. Antibacterial tests confirmed the activity of HPMC and CNF-based bionanocomposites against Gram-positive bacteria (*S. aureus*) due to released Zn^{2+}. Taking into account the results obtained in the current study, HPMC and CNF-based bionanocomposites loaded with 20% or 16.7% of hybrid, respectively, providing antibacterial activity while showing better mechanical properties than films with higher hybrid content, are the best candidates as potential dressings for application in wound healing.

CRediT authorship contribution statement

Esther Marugan: Methodology, Validation, Formal analysis, Investigation, Writing – original draft. **Ediana P. Rebitski:** Methodology, Investigation, Formal analysis. **Margarita Darder:** Conceptualization, Methodology, Investigation, Resources, Writing – review & editing, Supervision, Funding acquisition, Project administration. **Salvador R. G. Balestra:** Methodology, Investigation, Formal analysis, Writing – review & editing. **Gustavo del Real:** Methodology, Investigation, Formal analysis, Writing – review & editing. **Pilar Aranda:** Conceptualization, Methodology, Investigation, Resources, Writing – review & editing, Supervision, Funding acquisition, Project administration.

Declaration of Competing Interest

The authors declare that they have no known competing financial interests or personal relationships that could have appeared to influence the work reported in this paper.

Data availability

Data will be made available on request.

Acknowledgements

Authors acknowledge financial support from the MCIN/AEI/10.13039/501100011033 (Spain, project PID2019-105479RB-I00) and FEDER (EU) funds (project MAT2015-71117-R). We acknowledge support of the publication fee by the CSIC Open Access Publication Support Initiative through its Unit of Information Resources for Research (URICI). EPR acknowledges the CNPq (Brazil) for the fellowship 204360/2014-5. S. R. G. B. was supported by grant POSTDOC_21_00069 funded by Consejería de Universidad, Investigación e Innovación, Junta de Andalucía (Spain). We are thankful to C3UPO for the HPC facilities provided. Authors also acknowledge Dr. I Sobrados and Dr. V. Díez for valuable technical assistance and discussion in the NMR study.

Appendix A. Supplementary data

Supplementary data to this article can be found online at https://doi.org/10.1016/j.clay.2023.107002.

References

Abdul Khalil, H.P.S., Davoudpour, Y., Islam, M.N., Mustapha, A., Sudesh, K., Dungani, R., Jawaid, M., 2014. Production and modification of nanofibrillated cellulose using various mechanical processes: a review. Carbohydr. Polym. 99, 649–665. https://doi.org/10.1016/j.carbpol.2013.08.069.

Alam, M.J., Ahmad, S., 2015. FTIR, FT-Raman, UV–Visible spectra and quantum chemical calculations of allantoin molecule and its hydrogen bonded dimers. Spectrochim. Acta A Mol. Biomol. Spectrosc. 136, 961–978. https://doi.org/10.1016/j.saa.2014.09.119.

Alcântara, A.C.S., Darder, M., Aranda, P., Ayral, A., Ruiz-Hitzky, E., 2016. Bionanocomposites based on polysaccharides and fibrous clays for packaging applications. J. Appl. Polym. Sci. 133, 42362. https://doi.org/10.1002/app.42362.

Alcântara, A.C.S., Darder, M., Aranda, P., Ruiz-Hitzky, E., 2020. Zein-layered hydroxide biohybrids: strategies of synthesis and characterization. Materials 13, 825. https://doi.org/10.3390/ma13040825.

Amalraj, A., Gopi, S., Thomas, S., Haponiuk, J.T., 2018. Cellulose nanomaterials in biomedical, food, and nutraceutical applications: a review. Macromol. Symp. 380, 1800115. https://doi.org/10.1002/masy.201800115.

Araújo, L.U., Grabe-Guimarães, A., Mosqueira, V.C.F., Carneiro, C.M., Silva-Barcellos, N. M., 2010. Profile of wound healing process induced by allantoin. Acta Cir. Bras. 25, 460–466. https://doi.org/10.1590/S0102-86502010000500014.

Arizaga, G.G.C., Gardolinski, J.E.F. da C., Schreiner, W.H., Wypych, F., 2009. Intercalation of an oxalatooxoniobate complex into layered double hydroxide and layered zinc hydroxide nitrate. J. Colloid Interface Sci. 330, 352–358. https://doi.org/10.1016/j.jcis.2008.10.025.

Bannwarth, C., Ehlert, S., Grimme, S., 2019. GFN2-xTB—an accurate and broadly parametrized self-consistent tight-binding quantum chemical method with multipole electrostatics and density-dependent dispersion contributions. J. Chem. Theory Comput. 15, 1652–1671. https://doi.org/10.1021/acs.jctc.8b01176.

Bannwarth, C., Caldeweyher, E., Ehlert, S., Hansen, A., Pracht, P., Seibert, J., Spicher, S., Grimme, S., 2021. Extended tight-binding quantum chemistry methods. WIREs Comput. Mol. Sci. 11, e1493 https://doi.org/10.1002/wcms.1493.

Barahuie, F., Hussein, M.Z., Fakurazi, S., Zainal, Z., 2014. Development of drug delivery systems based on layered hydroxides for nanomedicine. Int. J. Mol. Sci. 15, 7750–7786. https://doi.org/10.3390/ijms15057750.

Becker, L.C., Bergfeld, W.F., Belsito, D.V., Klaassen, C.D., Marks, J.G., Shank, R.C., Slaga, T.J., Snyder, P.W., Andersen, F.A., 2010. Final report of the safety assessment of allantoin and its related complexes. Int. J. Toxicol. 29, 84S–97S. https://doi.org/10.1177/1091581810362805.

Boateng, J.S., Matthews, K.H., Stevens, H.N.E., Eccleston, G.M., 2008. Wound healing dressings and drug delivery systems: a review. J. Pharm. Sci. 97, 2892–2923. https://doi.org/10.1002/jps.21210.

Caldeweyher, E., Ehlert, S., Hansen, A., Neugebauer, H., Spicher, S., Bannwarth, C., Grimme, S., 2019. A generally applicable atomic-charge dependent London dispersion correction. J. Chem. Phys. 150, 154122 https://doi.org/10.1063/1.5090222.

Canada, T.A., Cowan, M.E., Wiencek, K.M., 2011. Wound Care Device Having Fluid Transfer Properties (Patent No. 8021685 B2).

Cazón, P., Vázquez, M., Velazquez, G., 2018. Cellulose-glycerol-polyvinyl alcohol composite films for food packaging: Evaluation of water adsorption, mechanical properties, light-barrier properties and transparency. Carbohydr. Polym. 195, 432–443. https://doi.org/10.1016/j.carbpol.2018.04.120.

Chemicalize, 2022. developed by ©2022 Chemaxon. https://chemicalize.com/. http://www.chemaxon.com. Accessed on January 2023.

Cunha, C.S., Castro, P.J., Sousa, S.C., Pullar, R.C., Tobaldi, D.M., Piccirillo, C., Pintado, M.M., 2020. Films of chitosan and natural modified hydroxyapatite as effective UV-protecting, biocompatible and antibacterial wound dressings. Int. J. Biol. Macromol. 159, 1177–1185. https://doi.org/10.1016/j.ijbiomac.2020.05.077.

Darder, M., Aranda, P., Ruiz-Hitzky, E., 2007. Bionanocomposites: a new concept of ecological, bioinspired, and functional hybrid materials. Adv. Mater. 19, 1309–1319. https://doi.org/10.1002/adma.200602328.

Darder, M., He, J., Charlet, L., Ruiz-Hitzky, E., Aranda, P., 2021. Gentamicin-montmorillonite intercalation compounds as an active component of hydroxypropylmethylcellulose bionanocomposite films with antimicrobial properties. Clay Clay Miner. 69, 576–588. https://doi.org/10.1007/s42860-021-00156-3.

Delahaye, E., Eyele-Mezui, S., Diop, M., Leuvrey, C., Rabu, P., Rogez, G., 2010. Rational synthesis of chiral layered magnets by functionalization of metal simple hydroxides with chiral and non-chiral Ni(II) Schiff base complexes. Dalton Trans. 39, 10577–10580. https://doi.org/10.1039/c0dt00834f.

Dharmalingam, K., Anandalakshmi, R., 2019. Fabrication, characterization and drug loading efficiency of citric acid crosslinked NaCMC-HPMC hydrogel films for wound healing drug delivery applications. Int. J. Biol. Macromol. 134, 815–829. https://doi.org/10.1016/j.ijbiomac.2019.05.027.

Dhivya, S., Padma, V.V., Santhini, E., 2015. Wound dressings - a review. BioMedicine 5, 24–28. https://doi.org/10.7603/s40681-015-0022-9.

Di, Z., Shi, Z., Ullah, M.W., Li, S., Yang, G., 2017. A transparent wound dressing based on bacterial cellulose whisker and poly(2-hydroxyethyl methacrylate). Int. J. Biol. Macromol. 105, 638–644. https://doi.org/10.1016/j.ijbiomac.2017.07.075.

Dubbeldam, D., Calero, S., Ellis, D.E., Snurr, R.Q., 2016. RASPA: molecular simulation software for adsorption and diffusion in flexible nanoporous materials. Mol. Simul. 42, 81–101. https://doi.org/10.1080/08927022.2015.1010082.

Elstner, M., Porezag, D., Jungnickel, G., Elsner, J., Haugk, M., Frauenheim, T., Suhai, S., Seifert, G., 1998. Self-consistent-charge density-functional tight-binding method for simulations of complex materials properties. Phys. Rev. B 58, 7260–7268. https://doi.org/10.1103/PhysRevB.58.7260.

Evans, D.G., Duan, X., 2006. Preparation of layered double hydroxides and their applications as additives in polymers, as precursors to magnetic materials and in biology and medicine. Chem. Commun. 5, 485–496. https://doi.org/10.1039/b510313b.

Fang, X., Mao, J., Cory, R.M., McKnight, D.M., Schmidt-Rohr, K., 2011. ^{15}N and ^{13}C{^{14}N} NMR investigation of the major nitrogen-containing segment in an aquatic fulvic acid: evidence for a hydantoin derivative. Magn. Reson. Chem. 49, 775–780. https://doi.org/10.1002/mrc.2816.

Ferreira, M.S., Sousa Lobo, J.M., Almeida, I.F., 2022. Sensitive skin: active ingredients on the spotlight. Int. J. Cosmet. Sci. 44, 56–73. https://doi.org/10.1111/ics.12754.

Figueiredo, M.P., Borrego-Sánchez, A., García-Villén, F., Miele, D., Rossi, S., Sandri, G., Viseras, C., Constantino, V.R.L., 2020. Polymer/iron-based layered double hydroxides as multifunctional wound dressings. Pharmaceutics 12, 1–18. https://doi.org/10.3390/pharmaceutics12111130.

Figueiredo, M.P., Lini, B., García-Villén, F., Borrego-Sánchez, A., Rossi, A., Viseras, C., Constantino, V.R.L., 2022. Innovative membrane containing iron-based layered double hydroxide intercalated with phyto therapeutic diterpenoid. Appl. Clay Sci. 216, 106358 https://doi.org/10.1016/j.clay.2021.106358.

Fillat, Ú., Wicklein, B., Martín-Sampedro, R., Ibarra, D., Ruiz-Hitzky, E., Valencia, C., Sarrión, A., Castro, E., Eugenio, M.E., 2018. Assessing cellulose nanofiber production from olive tree pruning residue. Carbohydr. Polym. 179, 252–261. https://doi.org/10.1016/j.carbpol.2017.09.072.

García-Villén, F., Souza, I.M.S., de Melo Barbosa, R., Borrego-Sánchez, A., Sánchez-Espejo, R., Ojeda-Riascos, S., Iborra, C.V., 2020. Natural inorganic ingredients in wound healing. Curr. Pharm. Des. 26, 621–641. https://doi.org/10.2174/1381612826666200113162114.

González del Campo, M.M., Darder, M., Aranda, P., Akkari, M., Huttel, Y., Mayoral, A., Bettini, J., Ruiz-Hitzky, E., 2018. Functional hybrid nanopaper by assembling nanofibers of cellulose and sepiolite. Adv. Funct. Mater. 28, 1703048. https://doi.org/10.1002/adfm.201703048.

Gonzalez, J.S., Ludueña, L.N., Ponce, A., Alvarez, V.A., 2014. Poly(vinyl alcohol)/cellulose nanowhiskers nanocomposite hydrogels for potential wound dressings. Mater. Sci. Eng. C 34, 54–61. https://doi.org/10.1016/j.msec.2013.10.006.

Gordeeva, A., Hsu, Y.-J., Jenei, I.Z., Brant Carvalho, P.H.B., Simak, S.I., Andersson, O., Häussermann, U., 2020. Layered zinc hydroxide dihydrate, $Zn_5(OH)_{10}{\cdot}2H_2O$, from hydrothermal conversion of ε-$Zn(OH)_2$ at gigapascal pressures and its transformation to nanocrystalline ZnO. ACS Omega 5, 17617–17627. https://doi.org/10.1021/acsomega.0c02075.

Grimme, S., Hansen, A., Ehlert, S., Mewes, J.-M., 2021. r^{2}SCAN-3c: a "Swiss army knife" composite electronic-structure method. J. Chem. Phys. 14 (154), 064103 https://doi.org/10.1063/5.0040021.

Hourahine, B., Aradi, B., Blum, V., Bonafé, F., Buccheri, A., Camacho, C., Cevallos, C., Deshaye, M.Y., Dumitrică, T., Dominguez, A., Ehlert, S., Elstner, M., van der Heide, T., Hermann, J., Irle, S., Kranz, J.J., Köhler, C., Kowalczyk, T., Kubař, T., Lee, I.S., Lutsker, V., Maurer, R.J., Min, S.K., Mitchell, I., Negre, C., Niehaus, T.A., Niklasson, A.M.N., Page, A.J., Pecchia, A., Penazzi, G., Persson, M.P., Řezáč, J., Sánchez, C.G., Sternberg, M., Stöhr, M., Stuckenberg, F., Tkatchenko, A., Yu, V.W.-Z., Frauenheim, T., 2020. DFTB+, a software package for efficient approximate density functional theory based atomistic simulations. J. Chem. Phys. 152, 124101 https://doi.org/10.1063/1.5143190.

Hussein, M.Z., Rahman, N.S.S.A., Sarijo, S.H., Zainal, Z., 2012. Herbicide-intercalated zinc layered hydroxide nanohybrid for a dual-guest controlled release formulation. Int. J. Mol. Sci. 13, 7328–7342. https://doi.org/10.3390/ijms13067328.

Isogai, A., Saito, T., Fukuzumi, H., 2011. TEMPO-oxidized cellulose nanofibers. Nanoscale 3, 71–85. https://doi.org/10.1039/C0NR00583E.

Jin, S.G., Yousaf, A.M., Kim, K.S., Kim, D.W., Kim, D.S., Kim, J.K., Yong, C.S., Youn, Y.S., Kim, J.O., Choi, H.-G., 2016. Influence of hydrophilic polymers on functional properties and wound healing efficacy of hydrocolloid based wound dressings. Int. J. Pharm. 501, 160–166. https://doi.org/10.1016/j.ijpharm.2016.01.044.

Kanikireddy, V., Varaprasad, K., Jayaramudu, T., Karthikeyan, C., Sadiku, R., 2020. Carboxymethyl cellulose-based materials for infection control and wound healing: a review. Int. J. Biol. Macromol. 164, 963–975. https://doi.org/10.1016/j.ijbiomac.2020.07.160.

Klippel, A.P., Margraf, H.W., 1974. Anti-microbial Compositions Utilizing Allantoin Compounds and Complexes (Patent No. 3,830,908). https://patents.google.com/patent/US3830908A/en.

Koehler, J., Brandl, F.P., Goepferich, A.M., 2018. Hydrogel wound dressings for bioactive treatment of acute and chronic wounds. Eur. Polym. J. 100, 1–11. https://doi.org/10.1016/j.eurpolymj.2017.12.046.

Kuş, N., Bayarı, S.H., Fausto, R., 2009. Thermal decomposition of allantoin as probed by matrix isolation FTIR spectroscopy. Tetrahedron 65, 9719–9727. https://doi.org/10.1016/j.tet.2009.09.088.

Kuznetsova, T.A., Andryukov, B.G., Besednova, N.N., Zaporozhets, T.S., Kalinin, A.V., 2020. Marine algae polysaccharides as basis for wound dressings, drug delivery, and tissue engineering: a review. J. Mar. Sci. Eng. 8, 481. https://doi.org/10.3390/JMSE8070481.

Lehmann, S.V., Hoeck, U., Breinholdt, J., Olsen, C.E., Kreilgaard, B., 2006. Characterization and chemistry of imidazolidinyl urea and diazolidinyl urea. Contact Derm. 54, 50–58.

León-Vallejo, A.M., Velázquez-Herrera, F.D., Sampieri, Á., Landeta-Cortés, G., Fetter, G., 2019. Study of layered double hydroxides as bactericidal materials against Corynebacterium ammoniagenes, a bacterium responsible for producing bad odors from human urine and skin infections. Appl. Clay Sci. 180, 105194 https://doi.org/10.1016/j.clay.2019.105194.

Li, J.H., Liu, X.R., Zhang, Y., Tian, F.F., Zhao, G.Y., Yu, Q.L.Y., Jiang, F.L., Liu, Y., 2012. Toxicity of nano zinc oxide to mitochondria. Toxicol. Res. 1, 137–144. https://doi.org/10.1039/c2tx20016c.

Liang, Y., He, J., Guo, B., 2021. Functional hydrogels as wound dressing to enhance wound healing. ACS Nano 15, 12687–12722. https://doi.org/10.1021/acsnano.1c04206.

Lisuzzo, L., Wicklein, B., Lo Dico, G., Lazzara, G., Del Real, G., Aranda, P., Ruiz-Hitzky, E., 2020. Functional biohybrid materials based on halloysite, sepiolite and cellulose nanofibers for health applications. Dalton Trans. 49, 3830–3840. https://doi.org/10.1039/c9dt03804c.

Madej, D., 2018. Examination of dehydration and dehydroxylation of synthetic layered (oxy)hydroxides through thermal analysis (TG-DSC-EGA-MS) and a discussion to the second Pauling's rule. Inorg. Chim. Acta 482, 402–410. https://doi.org/10.1016/j.ica.2018.06.047.

Martín-Sampedro, R., Eugenio, M.E., Ibarra, D., Ruiz-Hitzky, E., Aranda, P., Darder, M., 2022. Tailoring the properties of nanocellulose-sepiolite hybrid nanopapers by

varying the nanocellulose type and clay content. Cellulose 29, 5265–5287. https://doi.org/10.1007/s10570-022-04565-y.
Maver, T., Hribernik, S., Mohan, T., Smrke, D.M., Maver, U., Stana-Kleinschek, K., 2015. Functional wound dressing materials with highly tunable drug release properties. RSC Adv. 5, 77873–77884. https://doi.org/10.1039/c5ra11972c.
Mi, F.-L., Shyu, S.-S., Wu, Y.-B., Lee, S.-T., Shyong, J.-Y., Huang, R.-N., 2001. Fabrication and characterization of a sponge-like asymmetric chitosan membrane as a wound dressing. Biomaterials 22, 165–173. https://doi.org/10.1016/S0142-9612(00)00167-8.
Mohsin, S.M.N., Hussein, M.Z., Sarijo, S.H., Fakurazi, S., Arulselvan, P., Hin, T.Y.Y., 2013. Synthesis of (cinnamate-zinc layered hydroxide) intercalation compound for sunscreen application. Chem. Cent. J. 7, 26. https://doi.org/10.1186/1752-153X-7-26.
Moreira, N.H., Dolgonos, G., Aradi, B., da Rosa, A.L., Frauenheim, T., 2009. Toward an Accurate Density-Functional Tight-Binding Description of Zinc-Containing Compounds. J. Chem. Theory Comput. 5, 605–614. https://doi.org/10.1021/ct800455a.
Nabipour, H., Hu, Y., 2022. Layered zinc hydroxide as vehicle for drug delivery systems: a critical review. J. Porous. Mater. 29, 341–356. https://doi.org/10.1007/s10934-021-01171-4.
Neese, F., 2022. Software update: the ORCA program system—Version 5.0. WIREs Comput. Mol. Sci. 12, 5, e1606 https://doi.org/10.1002/wcms.1606.
Nyalosaso, J.L., Boonsin, R., Vialat, P., Boyer, D., Chadeyron, G., Mahiou, R., Leroux, F., 2019. Towards rare-earth-free white light-emitting diode devices based on the combination of dicyanomethylene and pyranine as organic dyes supported on zinc single-layered hydroxide. Beilstein J. Nanotechnol. 10, 760–770. https://doi.org/10.3762/BJNANO.10.75.
Perioli, L., Dorigato, A., Pagano, C., Leoni, M., Pegoretti, A., 2019. Thermo-mechanical and adhesive properties of polymeric films based on ZnAl-hydrotalcite composites for active wound dressings. Polym. Eng. Sci. 59, E112–E119. https://doi.org/10.1002/pen.24877.
Pickart, L.R., 1995. Allantoin-metal Complexes for Skin and Hair (Patent No. WO/1995/026194). https://patentscope.wipo.int/search/en/detail.jsf?docId=WO1995026194.
Portela, R., Leal, C.R., Almeida, P.L., Sobral, R.G., 2019. Bacterial cellulose: a versatile biopolymer for wound dressing applications. Microb. Biotechnol. 12, 586–610. https://doi.org/10.1111/1751-7915.13392.
Poul, L., Jouini, N., Fiévet, F., 2000. Layered hydroxide metal acetates (Metal = Zinc, Cobalt, and Nickel): Elaboration via hydrolysis in polyol medium and comparative study. Chem. Mater. 12, 3123–3132. https://doi.org/10.1021/cm991179j.
Pracht, P., Bauer, C.A., Grimme, S., 2017. Automated and efficient quantum chemical determination and energetic ranking of molecular protonation sites. J. Comput. Chem. 38, 2618–2631. https://doi.org/10.1002/jcc.24922.
Pracht, P., Bohle, F., Grimme, S., 2020. Automated exploration of the low-energy chemical space with fast quantum chemical methods. Phys. Chem. Chem. Phys. 22, 7169–7192. https://doi.org/10.1039/C9CP06869D.
Rappe, A.K., Casewit, C.J., Colwell, K.S., Goddard III, W.A., Skiff, W.M., 1992. UFF, a full periodic table force field for molecular mechanics and molecular dynamics simulations. J. Am. Chem. Soc. 114, 10024–10035. https://doi.org/10.1021/ja00051a040.
Rashed, A.N., Afifi, F.U., Shaedah, M., Taha, M.O., 2004. Investigation of the active constituents of *Portulaca oleraceae* L. (Portulacaceae) growing in Jordan. Pak. J. Pharm. Sci. 17, 37–45.
Rashki, S., Shakour, N., Yousefi, Z., Rezaei, M., Homayoonfal, M., Khabazian, E., Atyabi, F., Aslanbeigi, F., Safaei Lapavandani, R., Mazaheri, S., Hamblin, M.R., Mirzaei, H., 2021. Cellulose-based nanofibril composite materials as a new approach to fight bacterial infections. Front. Bioeng. Biotechnol. 9, 732461 https://doi.org/10.3389/fbioe.2021.732461.
Rebitski, E.P., 2020. Clay-Based Hybrid Nanoplatforms: Preparation, Characterization and Evaluation of Properties for Controlled Release of Bioactive Species. PhD Dissertation.. Autonomous University of Madrid http://hdl.handle.net/10486/692046.
Riduan, S.N., Zhang, Y., 2021. Recent advances of zinc-based antimicrobial materials. Chem. Asian J. 16, 2588–2595. https://doi.org/10.1002/asia.202100656.
Rogez, G., Massobrio, C., Rabu, P., Drillon, M., 2011. Layered hydroxide hybrid nanostructures: a route to multifunctionality. Chem. Soc. Rev. 40, 1031–1058. https://doi.org/10.1039/c0cs00159g.
Ruiz-Hitzky, E., Aranda, P., Darder, M., 2008. Bionanocomposites. In: Kirk-Othmer Encyclopedia of Chemical Technology. https://doi.org/10.1002/0471238961.bionruiz.a01 (Ed.).
Saghazadeh, S., Rinoldi, C., Schot, M., Kashaf, S.S., Sharifi, F., Jalilian, E., Nuutila, K., Giatsidis, G., Mostafalu, P., Derakhshandeh, H., Yue, K., Swieszkowski, W., Memic, A., Tamayol, A., Khademhosseini, A., 2018. Drug delivery systems and materials for wound healing applications. Adv. Drug Deliv. Rev. 127, 138–166. https://doi.org/10.1016/j.addr.2018.04.008.
Saito, T., Isogai, A., 2004. TEMPO-mediated oxidation of native cellulose. The effect of oxidation conditions on chemical and crystal structures of the water-insoluble fractions. Biomacromolecules 5, 1983–1989. https://doi.org/10.1021/bm0497769.
Saito, T., Kimura, S., Nishiyama, Y., Isogai, A., 2007. Cellulose nanofibers prepared by TEMPO-mediated oxidation of native cellulose. Biomacromolecules 8, 2485–2491. https://doi.org/10.1021/bm0703970.
Si, S., Taubert, A., Mantion, A., Rogez, G., Rabu, P., 2012. Peptide-intercalated layered metal hydroxides: effect of peptide chain length and side chain functionality on structural, optical and magnetic properties. Chem. Sci. 3, 1945–1957. https://doi.org/10.1039/c2sc01087a.
Siddiqi, K.S., ur Rahman, A., Tajuddin Husen, A., 2018. Properties of zinc oxide nanoparticles and their activity against microbes. Nanoscale Res. Lett. 13, 141. https://doi.org/10.1186/s11671-018-2532-3.
Sigalov, G., Fenley, A., Onufriev, A., 2006. Analytical electrostatics for biomolecules: beyond the generalized born approximation. J. Chem. Phys. 124, 124902 https://doi.org/10.1063/1.2177251.
Smith, A.M., Moxon, S., Morris, G.A., 2016. Biopolymers as wound healing materials. In: Ågren, M.S. (Ed.), Wound Healing Biomaterials. Woodhead Publishing, Duxford, UK, pp. 261–287. https://doi.org/10.1016/B978-1-78242-456-7.00013-1.
Stavitskaya, A., Batasheva, S., Vinokurov, V., Fakhrullina, G., Sangarov, V., Lvov, Y., Fakhrullin, R., 2019. Antimicrobial applications of clay nanotube-based composites. Nanomaterials 9, 708. https://doi.org/10.3390/nano9050708.
Tarrahi, R., Khataee, A., Karimi, A., Yoon, Y., 2022. The latest achievements in plant cellulose-based biomaterials for tissue engineering focusing on skin repair. Chemosphere 288, 132529. https://doi.org/10.1016/j.chemosphere.2021.132529.
Theiss, F.L., Ayoko, G.A., Frost, R.L., 2013. Thermogravimetric analysis of selected layered double hydroxides. J. Therm. Anal. Calorim. 112, 649–657. https://doi.org/10.1007/s10973-012-2584-z.
Vowden, K., Vowden, P., 2017. Wound dressings: principles and practice. Surgery (Oxford) 35, 489–494. https://doi.org/10.1016/j.mpsur.2017.06.005.
Xu, R., Xia, H., He, W., Li, Z., Zhao, J., Liu, B., Wang, Y., Lei, Q., Kong, Y., Bai, Y., Yao, Z., Yan, R., Li, H., Zhan, R., Yang, S., Luo, G., Wu, J., 2016. Controlled water vapor transmission rate promotes wound-healing via wound re-epithelialization and contraction enhancement. Sci. Rep. 6, 24596. https://doi.org/10.1038/srep24596.
Yu, J., Wang, Q., O'Hare, D., Sun, L., 2017. Preparation of two dimensional layered double hydroxide nanosheets and their applications. Chem. Soc. Rev. 46, 5950–5974. https://doi.org/10.1039/c7cs00318h.